

Assessment of a Wake Vortex Retrieval Method Using Large-Eddy Simulations and a Lidar Simulator

NIKLAS WARTHA^{a,b}, ANTON STEPHAN,^a AND FRANK HOLZÄPFEL^a

^a *Institut für Physik der Atmosphäre, Deutsches Zentrum für Luft- und Raumfahrt, Oberpfaffenhofen, Germany*

^b *Institute of Aerospace Systems, RWTH Aachen University, Aachen, Germany*

(Manuscript received 13 July 2024, in final form 9 October 2024, accepted 9 December 2024)

ABSTRACT: Wake vortex studies using light detection and ranging (lidar) measurements constitute a decisive element for determining appropriate and efficient aircraft separations. Algorithms for characterizing the position and strength of wake vortices within lidar scans are available, for example, the radial velocity (RV) method. However, due to the lack of a ground truth from field measurements, no reliable accuracy bound for these algorithms could be given so far. Thus, we perform virtual lidar measurements via large-eddy simulation (LES) lidar simulators (LLSs) employing high-fidelity LESs of landing aircraft, where the position and strength of vortices is fully known. Lidar measurements are simulated to realistic detail by including spatial averaging along a line-of-sight and flow field distortions caused by the measurement geometry. Previous studies either focused on the wake vortex simulation or the lidar simulation, but never both aspects in full detail. Through simulations under various atmospheric conditions, the accuracy of the RV method can be defined as a 4% strength overestimation and 6% dislocation for vortices within an altitude range of below 2.5 initial vortex separations. Within a highly turbulent atmosphere, the RV method performs worse. The main driver of RV method inaccuracy is revealed as the lack of modeling mirror vortices, i.e., imaginary vortices caused by walls. This work enables rating the accuracy of studies by employing the RV method realistically. Furthermore, the LLSs allow generating a labeled dataset for evaluating further algorithms and developing new ones which may increase the data accuracy and thus reduce the effort of costly field measurements.

SIGNIFICANCE STATEMENT: When employing algorithms for characterizing wake vortices in light detection and ranging (lidar) field measurements, the truth is not known, such that the accuracy of these characterizations remains highly speculative. In this work, we therefore simulate wake vortices through high-fidelity simulations of landing aircraft, where the state of the wake vortices can be determined with high accuracy at any point in time. By furthermore virtually installing true-to-life lidars, we are able to obtain simulated lidar scans with an available ground truth. For the first time, these high-quality simulated scans allow evaluating the accuracy of characterization algorithms for wake vortices. Additionally, the simulations deliver a comprehensive labeled dataset of lidar scans for future studies.


KEYWORDS: Vortices; Lidars/Lidar observations; Large eddy simulations

1. Introduction

Aircraft wake vortices are operationally relevant flow phenomena for all phases of flight. They are unavoidable by-products generated by any flying aircraft (Gerz et al. 2002) and can pose an invisible hazard to the following aircraft landing on that same runway (Zheng and Ash 1996; Holzäpfel and Steen 2007; Stephan et al. 2013; Holzäpfel et al. 2016). Wake vortices may be safety critical during all flight conditions; however, during approach and landing, the risk of a wake vortex encounter is most prominent: Aircraft are closely spaced and share similar glide paths (GPs), and their generated wake vortices interact with the ground, resulting in a boundary layer with detaching secondary vortices (Hallock and Holzäpfel 2018). Additional atmospheric conditions, particularly weak crosswinds,

may cause the generated wake vortices of a landing aircraft to stall above the runway (Stephan et al. 2013). Some required pilot reaction times for avoiding fatal incidents at low altitudes are beyond human capability. Wake vortex safety considerations were first implemented in flight operations in the 1970s, when the International Civil Aviation Organization (ICAO) increased the minimum landing separation from the minimum radar separation for certain ICAO leader-follower aircraft pairs (Gerz et al. 2002).

With these separations of landing aircraft, the throughput at airports is limited. Since the introduction of the separation minima, flight demand has continuously increased, and also in the future, air traffic is expected to grow further (EUROCONTROL 2022). Thus, for economical reasons, several new separation programs have been suggested and introduced in the past years. For instance, a time-based separation approach (De Visscher et al. 2020) has been introduced at London Heathrow Airport (Morris et al. 2013), and phase 1 of the European Wake Vortex Recategorisation (RECAT-EU) program (RECAT-1) (Rooseleer and Treve 2018) has been introduced at several airports, such as Paris Charles de Gaulle Airport (Ministère de la Transition Écologique et Solidaire 2018). RECAT-2 considers

 Denotes content that is immediately available upon publication as open access.

Corresponding author: Niklas Wartha, niklas.wartha@dlr.de

DOI: 10.1175/JTECH-D-24-0093.1

© 2025 Author(s). This published article is licensed under the terms of a Creative Commons Attribution 4.0 International (CC BY 4.0) License



individual aircraft type pair separations, and RECAT-3 ultimately aims at dynamic pairwise separations considering the effects of the prevailing atmospheric conditions on wake vortex behavior. For realizing these novel separation programs, both theoretical and experimental studies are necessary, evaluating the feasibility, the potential benefit, and maintenance of safety. Equally, wake vortex monitoring plays an important role for urban air mobility (UAM) operations of vertiports in the airport vicinity. In this work, we focus on experimental wake vortex studies, which are commonly performed with light detection and ranging (lidar) instruments in cloud-free conditions (Barbaresco et al. 2015; Oude Nijhuis et al. 2018).

Prerequisite for successfully assessing potential wake vortex hazards is the knowledge of vortex position and strength. A suitable measure for the vortex strength is its circulation Γ (Holzäpfel et al. 2003; Hinton and Tatnall 1997), computed by integrating the tangential velocity \mathbf{V} along a line s which by Stokes' theorem equals the integral of the vorticity in flight direction ω_x over the enclosed surface \mathbf{A} :

$$\Gamma = \oint_{\partial A} \mathbf{V} \cdot d\mathbf{s} = \int_A \omega_x dA. \quad (1)$$

Particularly, the mean vortex circulation obtained over the radii range 5–15 m, expressed as $\Gamma_{5-15} = 0.1 \int_{5m}^{15m} \Gamma(r) dr$, is a standard parameter in judging the potential threat of wake vortices for aircraft (Gerz et al. 2002). Extracting the key vortex characteristics, position, and circulation from lidar measurements is not trivial as no two-dimensional velocity data, but solely the line-of-sight (LOS) velocity (one-dimensional) along the laser beam are available. Several algorithms have been developed for processing both key characteristics from lidar measurements, involving physical and data-driven processing algorithms. An exemplary and prevalent physical processing algorithm is the radial velocity (RV) method developed by Smalikho et al. (2015), whereas an exemplary data-driven processing algorithm is the convolutional neural network (CNN) model developed by Wartha et al. (2022). A combined physical and data-driven processing algorithm was recently presented (Stephan et al. 2023). Physical processing algorithms are theoretically well understood and have been widely applied throughout measurement campaigns such as at Vienna International Airport (Holzäpfel et al. 2021). The advantage of the physical processing algorithms is their physical explainability and theoretical accuracy (systematic error). On the other hand, they often show limiting performance in turbulent atmospheric conditions. In these situations, their true accuracy is yet to be investigated (Smalikho 2019). Field measurements indicate that the theoretical accuracy of the RV method (Smalikho et al. 2015; Smalikho 2019) likely underestimates the true error bound of the method significantly. Furthermore, data-driven processing algorithms are hindered in flourishing their true potential as their supervised nature requires a physical processing algorithm, such as the RV method, to train the machine learning (ML) models. Labels by the physical processing algorithm carry their inherent errors directly into the training process of the ML models.

Unlike with field measurements, three-dimensional velocity data as well as all other relevant flow parameters are available when performing wake vortex simulations. Within the wake vortex simulations, virtual lidar can be modeled, providing a comprehensive wake vortex lidar dataset. Simulations of atmospheric measurement instruments in the context of wake vortex detection initiated in the 1970s (Thomson and Meng 1976), branching off to onboard configurations and ground configuration, suiting our purpose. Within this field, studies either focus on fully simulating the operating of a lidar or on simulating wake vortices in full detail. It started with the former where white noise or random backscatter spectra were assumed (Rye 1990). Half a decade later, Salamitou et al. (1995) investigated different atmospheric conditions, altering the backscatter spectrum accordingly, and Frehlich (1997) analyzed the condition's effect on the lidar performance. The focus on the wake vortex simulation in the context of lidar simulations was, to the authors' knowledge, first done by Holzäpfel et al. (2003), where Navier–Stokes numerical simulations of a Lamb–Oseen vortex pair (Lamb 1923) and an aircraft generated multivortex system were performed. However, lidar simulations were focused on kinematic wake vortex characteristics and lidar geometry. Frehlich and Sharman (2005) added lidar parameters such as range gate, angle scan rate, wavelength, and pulse duration. Further lidar scanning, processing, and atmospheric scattering parameters were simulated in a large-eddy simulation (LES) by Wassaf et al. (2011) and Jacob et al. (2015). Still today, lidar simulations for wake vortex characterization are performed with various levels of detail. Typically, the simulated lidar is the focus of the studies, as in Lugan (2016), Gao et al. (2018, 2019), Li et al. (2020), and Wei et al. (2024), or the generation of the wake vortices with high-fidelity aircraft simulations (Stephan et al. 2019a). Each approach is typically limited by the incompleteness of the other aspect.

This paper, therefore, has the aim to join the two aspects, by implementing virtual lidar instruments including the most crucial lidar parameters for geometry and operation and planting these into high-fidelity wake vortex simulations. This allows us to evaluate the accuracy of the RV method, contextualizing previous studies and further facilitating the development of increasingly advanced data-driven processing algorithms for the characterization of wake vortices. The objective is to develop virtual lidars within high-fidelity hybrid Reynolds-averaged Navier–Stokes (RANS) and LESs of landing aircraft. The therefore called LES lidar simulator (LLS) enables the assessment of virtual lidar scans using the RV method and comparing the vortex characteristic estimates to the simulation truth (ST), which under certain limits we consider to be the ground truth as the three-dimensional field of all relevant flow parameters is available in the simulations for evaluating the position and strength of the wake vortices.

The remainder of this paper is structured as follows: In section 2a, lidar operating for wake vortices and the RV method are outlined; thereafter, section 2b describes the underlying numerical simulations. The LLS is introduced in section 2c. In section 3a, we establish the validity of the numerical simulations. The analysis continues with discussing the LLS measurements in section 3b. Finally, in section 3c, we compute and segment RV

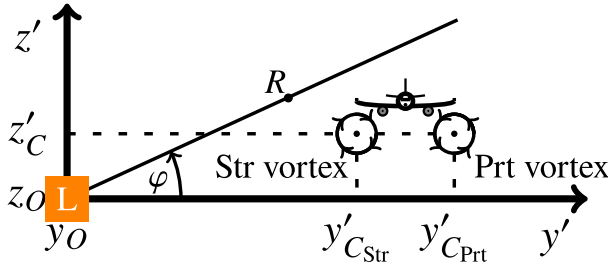


FIG. 1. Lidar performing RHI scans perpendicular to the runway, with an aircraft flying out of the page, generating a starboard (Str) and a port (Prt) vortex at $(y'_{C_{Str}}, z'_{C_{Str}})$ and $(y'_{C_{Prt}}, z'_{C_{Prt}})$, respectively (in the lidar coordinate system). The “L” represents the lidar at (y_0, z_0) (in the numerical simulation coordinate system) with its beam given by the solid black line and (R, φ) giving the position of a measurement point (Wartha et al. 2022).

method accuracy levels. Note that a precursor of this paper has been presented at the 2023 American Institute of Aeronautics and Astronautics (AIAA) Aviation Forum in San Diego (Wartha et al. 2023).

2. Methods

a. Pulsed coherent Doppler lidar principles

1) MEASURING WAKE VORTICES

Pulsed coherent Doppler lidars (PCDLs) have become the instrument of choice for measuring wake vortices with a high spatial resolution at airports. PCDLs and lidars are used interchangeably in this paper. Typically, range–height indicator (RHI) scans are conducted perpendicular to the airport runway. Figure 1 illustrates an emitted laser beam from the lidar. Upon interaction with the aerosols (air particles) in the atmosphere, a backscatter is received from which aerosol motion at different ranges (distances) R from the lidar can be detected from the spectrum of Doppler shifts in frequency. Aerosols approaching and moving away from the lidar are associated with negative and positive LOS velocities V_r , respectively. During an RHI scan, the LOS continuously changes its elevation angle φ at a predetermined scanning rate ω_S between a minimal and maximal elevation angle φ_- and φ_+ , respectively. Once φ_- or φ_+ has been reached, ω_S is reversed, and a new RHI scan is initiated. RHI lidar scans consist of LOS velocities recorded at (R, φ) in a polar coordinate system. The lidar coordinate system is referred to with a dash (') in this paper.

Deducing LOS velocities from the aerosol movement in the atmosphere with a PCDL cannot be achieved with point measurements. Instead, a PCDL makes use of the LOS velocities V_r of scattering aerosols within a sensing volume, which differ due to ever-present turbulence in the atmosphere. The following derivation is based on Banakh and Smalikho (2013, chapters 1–2), unless claimed otherwise. The sensing volume is limited to the longitudinal LOS direction, as it greatly exceeds the beamwidth. With the aid of a weighting function Q_S (discussed below), which is convoluted with the various V_r

measurements, the LOS velocity averaged over the sensing volume along the LOS,

$$\bar{V}_r(R) = \int_{-\infty}^{+\infty} Q_S(s) V_r(R + s) ds, \quad (2)$$

can be obtained. The above assumes a single laser pulse, which under the assumption of no instrument noise, appropriate for assessing systematic errors, suffices (Frehlich et al. 1997; 2006). Additionally, effects related to varying aerosol types, distributions, etc. are neglected (Robey and Lundquist 2022). The Doppler relation,

$$\bar{V}_r = \frac{\lambda \bar{f}_r}{2}, \quad (3)$$

utilizes the laser wavelength λ to extract velocity information from the frequency domain, as well as the averaged frequency shift \bar{f}_r between the emitted and backscatter signal, which is obtained from,

$$\bar{f}_r = \bar{P}_S^{-1} \int_{-\infty}^{+\infty} f \bar{S}_S(f) df, \quad (4)$$

where \bar{P}_S gives the average normalized power of the backscatter signal and \bar{S}_S is the average normalized spectrum of the backscatter.

The weighting function Q_S represents the spatial resolution along the LOS and thus dictates the contribution of aerosols in a sensing volume to the averaged LOS velocity associated with the sensing volume. The weighting function plays a substantial role in modeling the sampling procedure of a lidar (see section 2c) and is derived from two primary components. First, the pulse shape is considered. The power of a single Gaussian pulse,

$$P_P(t) = \frac{E_P}{\sqrt{\pi} \sigma_P} \exp\left(-\frac{t^2}{\sigma_P^2}\right), \quad (5)$$

is made up of the pulse energy E_P , and the pulse duration,

$$2\sigma_P = \frac{\tau_P}{\sqrt{\ln 2}}, \quad (6)$$

is determined by the power drop to the e^{-1} level from the peak. The pulse duration can also be defined by τ_P where the power drop to the half-maximum level from the peak is considered instead [full width at half maximum (FWHM)]. Second, the temporal window $W(t)$ corresponding to the range gate is considered. For a rectangular temporal window, the indicator function is employed:

$$W(t) = \begin{cases} 1, & |t| \leq T_W/2 \\ 0, & |t| > T_W/2, \end{cases} \quad (7)$$

where $T_W = \int_{-\infty}^{+\infty} |W(t)|^2 dt$ is the effective width of the time window. The combination of the range gate and pulse profiles can be represented by their convolution in the spatial domain

(Frehlich 1997; Robey and Lundquist 2022). The temporal lidar quantities can be converted to the spatial domain via the speed of light $c = 0.29979 \text{ m ns}^{-1}$. The result of this operation is the weighting function given by

$$Q_S(s) = \frac{1}{cT_W} \left[\operatorname{erf} \left(\frac{2s/c + T_W/2}{\sigma_P} \right) - \operatorname{erf} \left(\frac{2s/c - T_W/2}{\sigma_P} \right) \right], \quad (8)$$

where the standard error function is $\operatorname{erf}(x) = (2/\sqrt{\pi}) \int_0^x \exp(-\xi^2) d\xi$ and s gives the coordinate along the beam with respect to the range gate center. The associated physical resolution, or sensing volume length, is given by $\Delta z = (cT_W/2) / \operatorname{erf}[T_W/(2\sigma_P)]$.

2) CHARACTERIZING WAKE VORTICES

The RV method (Smalikho et al. 2015) is a well-regarded wake vortex characterization algorithm for PCDLs with $\lambda \approx 1.5 \mu\text{m}$ and was recently employed at a Vienna International Airport campaign (Holzäpfel et al. 2021). Elementary RV method considerations are recapitulated below. Note that further RV method developments exist (Smalikho 2019); however, we focus on evaluating the version employed by Holzäpfel et al. (2021). The ranges from the lidar to the vortex centers R_C are obtained by computing the maxima of

$$D(R_j) = \sum_{k=0}^K [\bar{V}_r(R_j, \varphi_k)]^2, \quad (9)$$

with the lidar scan consisting of K LOSs, each with J range gates. The elevation angles to the vortex centers φ_C are the mean between φ corresponding to the minimum and maximum \bar{V}_r at the previously identified R_C . The vortex circulations are computed by minimizing the functional

$$G(\Gamma_n) = \sum_{k=0}^K [\bar{V}_r(R_{C,n}, \varphi_k) - \tilde{V}_r(R_{C,n}, \varphi_k; \Gamma_1, \Gamma_2)]^2, \quad (10)$$

for fitting two vortices via the Burnham–Hallock vortex model (Burnham and Hallock 1982). The vortex circulations of both the starboard (Str) and the port (Prt) vortex ($n = 1, 2$) are estimated by minimizing the difference of the velocity arcs belonging to the two R_C between the measurements and models (indicated by tilde).

The flow field can be decomposed as a sum of the background wind and the turbulent field. Therefore, a radially averaged lidar RHI scan prior to the passage of the aircraft (without wake vortices) is subtracted from the scans. Although a temporal delay between the scans exists, temporally constant atmospheric structures such as crosswinds can be captured, and their influence on the characterization reduced.

b. Numerical wake vortex simulation methods

Four high-fidelity RANS–LES runs of the wake vortices generated by aircraft during final approach and landing under varying meteorological conditions are performed. Below key points of the method by Stephan et al. (2014) are recapitulated, particularly focusing on adaptations of their method.

Fundamental parameters of the wake vortex simulations are summarized in Table 1, detail follows in the below sections. Normalization parameters, the initial/root circulation Γ_0 , the initial vortex spacing b_0 , the initial vortex descend velocity w_0 , the characteristic time t_0 , and the vorticity unit ω_0 , assume an elliptic load distribution (Gerz et al. 2002). Parameters normalized throughout this paper are marked with an asterisk (*).

1) GOVERNING EQUATIONS

The incompressible Navier–Stokes code Multi Grid Large Eddy Turbulence (MGLET) (Manhart 2004) developed at the Technical University of Munich is employed for solving the Navier–Stokes and continuity equations:

$$\frac{\partial u_i}{\partial t} + \frac{\partial(u_i u_j)}{\partial x_j} = -\frac{1}{\rho} \frac{\partial p'}{\partial x_i} + \frac{\partial}{\partial x_j} [(\nu + \nu_t) 2S_{ij}], \quad (11)$$

$$\frac{\partial u_j}{\partial x_j} = 0, \quad (12)$$

where the velocity components for the three spatial directions $i = 1, 2$, and 3 are u_i , the strain rate tensor is denoted by $S_{ij} = (\partial u_i / \partial x_j + \partial u_j / \partial x_i) / 2$, the pressure deviation from a reference state p_0 is given by $p' = p - p_0$, and ρ is the air density. We employ the Lagrangian dynamic subgrid-scale model by Meneveau et al. (1996), from which the kinematic viscosity (sum of molecular viscosity ν and eddy viscosity ν_t) is computed. The above equations are solved with a fourth-order finite-volume compact scheme from Hokpunna and Manhart (2010), where the coefficients are obtained from a split-interface algorithm for the parallelization of the tridiagonal system (Hokpunna 2009). Time integration is performed with an explicit third-order Runge–Kutta algorithm.

2) RANS FLOW FIELD INTEGRATION

Performed simulations are one-directional RANS simulation and LES couplings, allowing the investigation of all wake vortex evolution phases (see Breitsamter 2007, chapter 2) in ground proximity: near field, extended near field (roll-up phase), mid-/far field (vortex phase), and decay phase. This coupling was first introduced by Misaka et al. (2012), with the addition to simulate landing aircraft by Stephan et al. (2014).

The RANS simulation is performed for a 1:27 model (reducing computational demand) of an Airbus A340 aircraft in high-lift configuration and a freestream velocity of $U_\infty = 25 \text{ m s}^{-1}$, with an aspect ratio $\Lambda = 9.3$ and a lift coefficient $C_L = 1.4$ using the Deutsches Zentrum für Luft- und Raumfahrt (DLR)'s TAU code (Schwamborn et al. 2006; Keye 2011). To achieve realistic wake vortex lidar scans, the RANS solution dimensions are scaled by a factor of 27, and a realistic flight speed of $U_\infty = 75 \text{ m s}^{-1}$ (Breitsamter 2007, page 34) is attained by scaling velocities by a factor of 3. This gives a wingspan of $B = 60.4 \text{ m}$. The scaling yields a realistic Reynolds number of $\text{Re} \approx 30 \times 10^6$ and leads to larger vortex core radii, which we assume relatively less significant in comparison to lidars mollifying high velocities and steep gradients of the vortex cores.

TABLE 1. Wake vortex simulation parameters. Aircraft parameters are quoted for the scale 1:1, whereas appropriately, the 1:27 model parameters are given in parentheses. Values used for normalization are marked with an asterisk, and their definition can be found in Gerz et al. (2002). Note that formulas are only given for actively computed parameters in this paper.

Parameter	Symbol	Unit	Formula	Value
Aircraft wingspan	B	m	—	60.4 (2.2)
Aircraft wing aspect ratio	Λ	—	—	9.3
Freestream velocity/true airspeed	U_∞	m s^{-1}	—	75 (25)
Lift coefficient	C_L	—	—	1.4
GP angle	γ	$^\circ$	—	3.6
Aircraft pitch angle	θ	$^\circ$	—	5.5
Initial/root circulation (*)	Γ_0	$\text{m}^2 \text{s}^{-1}$	$(2C_L U_\infty B)/(\pi\Lambda)$	433.9
Initial vortex spacing (*)	b_0	m	$(\pi/4)B$	47.4
Initial vortex descend velocity (*)	w_0	m s^{-1}	$\Gamma_0/(2\pi b_0)$	1.5
Characteristic time (*)	t_0	s	b_0/w_0	32.6
Vorticity unit (*)	ω_0	s^{-1}	$1/t_0$	0.03
Computational domain (normalized by b_0)	$[X^*, Y^*, Z^*]$	—	—	[23.3, 11.7, 2.9]
LES grid spacing (normalized by b_0)	$[dx^*, dy^*, dz^*]$	—	—	[0.011, 0.011, 0.011]
Crosswind strengths (normalized by w_0)	χ	—	—	0.0, 0.5, 1.0, 2.0

While the RANS simulation is carried out on a fine unstructured grid, the LES uses a structured grid. Steady RANS solutions are thus interpolated onto a Cartesian grid, which we call frames. We realize a glide path angle of 3.6° (for computational reasons slightly above the typical 3°), such that a shift of one vertical grid point in the equidistant LES grid requires a shift of 16 horizontal grid points. Keeping in mind the Courant–Friedrichs–Lewy condition, we halve the time step and, thus, need twice as many RANS frames, 32 in total. Two sets of RANS frames result, employed alternately. The flight speed of 75 m s^{-1} is met with the LES time step (Stephan 2014):

$$dt = \frac{0.5dx}{U_\infty} \sqrt{1 + \frac{1}{16^2}}. \quad (13)$$

Under crosswind conditions, a sideslip angle counters the wind-induced lateral velocity, ensuring touchdown on the runway— dt is adjusted accordingly.

The A340 landing is thus realized in two steps. First, wake initialization is performed in a RANS–LES run, where the RANS flow field represents a forcing term in the LES Navier–Stokes equations. Second, the forgoing simulation is temporally extended in pure LES for observing the long-term behavior of wake vortices.

3) BOUNDARY CONDITIONS AND COMPUTATIONAL DOMAIN

Side boundary conditions of the LES computational domain are periodic, such that vortices can be tracked for great lateral distances and avoid wall effects. The front and back boundary conditions are periodic for achieving an aircraft initialization which adheres to Helmholtz’s vortex theorems (Kundu and Cohen 2002, page 134) as described in Stephan et al. (2014). The bottom and top boundary conditions are non-slip to represent the ground and free-slip, respectively.

The LES computational domain is set to $[X^*, Y^*, Z^*] = [23.3, 11.7, 2.9]$ in flight, spanwise, and vertical directions,

respectively, avoiding significant interactions with the domain boundaries, given that measurements and simulations suggest vortex rebound to not climb beyond an altitude of $1.5b_0$ (Holzapfel et al. 2016) and $2.0b_0$ (Holzapfel et al. 2016), respectively. Furthermore, lateral wake vortex transport is limited to $4.5b_0$ (Holzapfel and Steen 2007) and $3.3b_0$ (Stephan et al. 2014) in measurements and simulations, respectively.

A fine and uniform grid spacing $dx^* = dy^* = dz^* = 0.011$ is used, resolving wake vortices with an adequate number of grid points. For instance, a vortex core of 2-m radius is resolved by the minimum of seven grid points.

In this work, both t^* and t_L^* are employed for temporal analysis. The former represents the vortex age; the initialization t_0^* is thus dependent on the longitudinal position of the lidar along the aircraft glide path. Instead, t_L^* allows comparison of lidars at different positions. The initialization $t_{L,0}^*$ occurs at the touchdown of the aircraft.

For reference, the following notes some key aircraft positions and times. On domain entrance, $x^* = 0$, the aircraft has an altitude of $z^* = 1.0$ and $t_L^* = -0.33$. The aircraft touches down at $x^* = 16.5$. Without crosswind, the aircraft glide path is located at $y^* = 0$, and with crosswinds, the aircraft glide path is located at $y^* = 2.8$ (upwind) in the computational domain, allowing longer vortex tracking.

4) AMBIENT TURBULENT WIND

Below an altitude of $1.5b_0$ (Robins et al. 2001), wake vortices induce vorticity of opposite sign onto the ground, creating a boundary layer (Harvey and Perry 1971). Once the pressure inside the boundary layer is high enough, secondary vortices detach and interact with the primary wake vortices, causing their diverging lateral transport and rebound (Zheng and Ash 1996; Spalart et al. 2001). When a crosswind is present, the lee (downwind) and luff (upwind) secondary vortices are strengthened and attenuated by the wind, respectively. In ground vicinity, a weak crosswind, matching the vortex-induced lateral propagation speed, $0.5w_0 = 0.73 \text{ m s}^{-1} \approx 1.4$ knots (kt; $1 \text{ kt} \approx 0.51 \text{ m s}^{-1}$) (“light air” on the Beaufort wind scale,

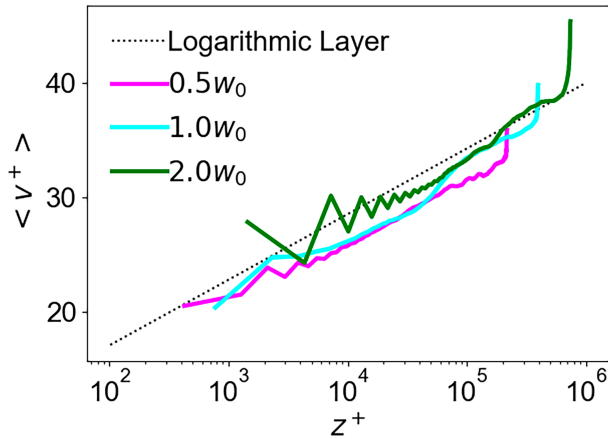


FIG. 2. Mean velocity profile in wind direction $\langle v^+ \rangle$ with respect to distance above the ground z^+ of fully developed crosswinds for three strengths χw_0 . The expected profile is given by the dashed line.

associative with “still air” conditions at airports) (Holzäpfel and Steen 2007; Stephan et al. 2013; Holzäpfel et al. 2016), can lead to the luff primary wake vortex remaining in the glide path for significant periods of time.

Wake vortex simulations of the landing A340 are performed in a quiescent atmosphere and for turbulent crosswinds at strengths of $0.5w_0$, $1.0w_0$, and $2.0w_0$. In the case without wind, no ambient turbulence is present. Studying a crosswind strength of $1.0w_0$ is operationally relevant; London Heathrow Airport records most wake vortex encounters at this crosswind strength (Critchley and Foot 1991). A crosswind strength of $2.0w_0$ is responsible for enhanced boundary layer turbulence, disturbing the coherency of wake vortices. Beyond $2.0w_0$ crosswinds, wake vortices advect quickly out of relevant runway areas, inhibiting serious wake vortex encounter threats.

For the crosswind cases, presimulations are performed, introducing turbulent velocity fluctuations and a physical boundary layer in the LES. The implementation is described in Stephan (2014), and below key steps are recapitulated. A typical half-channel flow is simulated (see e.g., Kundu and Cohen 2002, chapter 13.11) by imposing a pressure gradient dp/dy set such that the mean velocity of the wind at the altitude b_0 is the desired multiple χ of w_0 . In combination with the nonslip bottom boundary, a logarithmic vertical wind profile of $v^+(z^+) = \ln z^+/\kappa + B$ [$\kappa = 0.4$ is the von Kármán constant (Baumert 2013) and $B = 5.5$] is achieved once characteristic wall vorticity streaks establish and the mean vertical velocity profile $\langle v^+ \rangle = \bar{v}/u_\tau$ agrees with Moser et al. (1999), where $u_\tau = \sqrt{\bar{\tau}_w/\rho}$ is the wall friction velocity in the spanwise direction with $\bar{\tau}_w = -(d\bar{p}/dy)\delta$, $z^+ = (zu_\tau)/\nu = \text{Re}_\tau z/\delta$ is the nondimensional height, δ represents the half-channel width, and $\text{Re}_\tau = (u_\tau\delta)/\nu$ is the defining intrinsic Reynolds number.

Figure 2 confirms the adherence to the logarithmic turbulent boundary layer described by Moser et al. (1999). The simulated winds contain a marginal underestimation of the

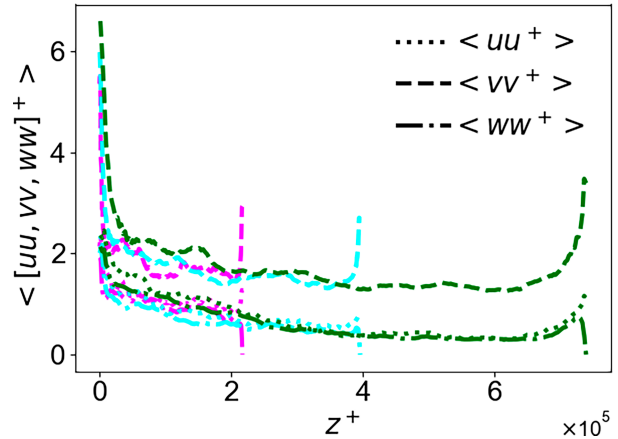


FIG. 3. Mean RMS fluctuations of all velocity components $[uu, vv, ww]^+$ with respect to distance above the ground z^+ of fully developed crosswinds for three strengths χw_0 . Line colors are analogous to Fig. 2.

average wind speed. The larger variability at low altitudes for the $2.0w_0$ case is caused by the vorticity streaks detaching due to high pressure gradients at higher wind speeds. Generally, the $2.0w_0$ case is inherent to higher turbulence as illustrated by the root-mean-square (RMS) of the velocity fluctuations in Fig. 3. The crosswind deviates from the logarithmic trend when approaching the free-slip boundary at the top of the computational domain. The presented wind statistics are satisfactory for the complex flow behind a landing aircraft, particularly when considering the sinking aircraft altitude throughout the simulation and the particularly large domain height—flow effects in this region are negligible for the wake vortex development.

5) LES VORTEX TRACKING

The ground truth position and circulation of the wake vortices in the LESs are obtained via a pressure–vorticity algorithm. The vorticity in flight direction ω_x and the pressure p suffice when vortices are strong enough, coherent, and tilting is limited (Hennemann 2010; Stephan 2014). Since RHI lidar scans are limited to flow field slices and also do not consider vortex tilting, the pressure–vorticity algorithm is allowed up until a limited degree of vortex tilting. Above this degree, using only ω_x for the characterization underestimates vortex circulation.

c. LLS method

Computationally feasible numerical wake vortex simulations in LES do not offer a sufficient spatial resolution for explicitly performing virtual measurements of scattering along a lidar beam (Robey and Lundquist 2022). Thus, the LLS method focuses on the volume averaging within the scanning volume of the lidar backscatter, by considering the range gates and pulse shape with a range gate weighting function (RWF) analogous to Eq. (8) (Simley et al. 2014; Lundquist et al. 2015;

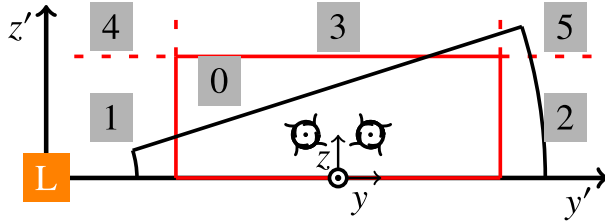


FIG. 4. Schematic of the lidar and LES coordinate systems. The LES domain is drawn in red, and the lidar measurement window is drawn in black. Field 0 represents the region where velocities can be retrieved from the appropriate location in the LES domain. Fields 1–5 represent regions where flow field padding is applied.

Meyer Forsting et al. 2017; Robey and Lundquist 2022) leading to the low-pass filter smoothing characteristic of a lidar.

This approach is appropriate when the LOS velocity can be estimated accurately via the center of gravity of the Doppler spectrum, which is valid for large signal-to-noise ratio (SNR) values (Banakh and Smalikho 2013, 1997; Frehlich 1997; Robey and Lundquist 2022). On the contrary, when the SNR is small (a great noise component exists), the position of the maximum in the Doppler spectrum allows the most accurate LOS velocity estimation (Stephan et al. 2019b). Although for a PCDL the SNR is typically small, we employ the idealized first approach to circumvent the computation and storage of spectral data. In this manner, we are able to estimate the accuracy of wake vortex processing algorithms, such as the RV method, excluding instrument noise.

1) LOS VELOCITY RETRIEVAL

The LLS directly computes LOS velocities. In the LESs, the flow velocity vector $\mathbf{V} = [u, v, w]$ is computed at each node and time step dt . The elevation angle change with the scanning rate ω_S is implemented by assuming that all velocities along one LOS are recorded at the same moment in time. LOSs are measured at discrete elevation angles $d\varphi$ and lidar time steps dt' (complied with ω_S). Since $dt \ll dt'$, the nearest-neighbor interpolation is used to select relevant LES time steps for the recording of LOS velocities. Along a single LOS, multiple LOS velocities must be computed. Bilinear interpolation is used to obtain \mathbf{V} from the LES grid. A LOS velocity is then obtained by projection of the velocity components onto the LOS unit direction vector \mathbf{e} :

$$V_r = \mathbf{e} \cdot \mathbf{V} = v \cos\varphi + w \sin\varphi. \quad (14)$$

Virtual lidars are installed perpendicular to the runway in the LES computational domain, i.e., $y||y'$; thus, the velocity component u can be disregarded for computing V_r . For computational efficiency, a padding method is implemented in less relevant regions of the lidar scans, where LOSs reach beyond the computational domain as sketched in Fig. 4. In field 0, values of \mathbf{V} are directly retrieved from the LES. In the horizontal regions outwith of the domain (fields 1 and 2), the z component of the desired measurement point remains unchanged, while the y component is changed to the lowest node in the

domain y_- and highest node in the domain y_+ , respectively. This selects \mathbf{V} at the domain boundaries to points of the same z . Similarly, field 3 operates in the vertical sense, selecting \mathbf{V} from y and z_+ . Last, fields 4 and 5 select values from (y_-, z_+) and (y_+, z_+) , respectively. A decreasing weighting factor is applied with increasing distance to the LES domain boundary, avoiding the stimulation of extreme velocities.

2) APPLICATION OF THE RWF

Equation (2) established that the individual LOS velocities of the aerosols in the scanning volume V_r and the RWF Q_S are crucial for determining the averaged LOS velocity over a sensing volume V_r along the LOS. Distance R spans from the lidar to the center of the sensing volume, J individual V_r are modeled about the center with equidistant points (spacing h) in a range $[-\hat{R}, +\hat{R}]$ along the LOS (Robey and Lundquist 2022). The quadrature formulation by Robey and Lundquist (2022),

$$\bar{V}_r(R) = \int_{-\infty}^{+\infty} Q_S(s)V_r(R+s)ds \approx \frac{\sum_j h_j Q_S(s_j)}{\sum_i h_i Q_S(s_i)} V_r(R+s_j), \quad (15)$$

is implemented. In section 2a, we established that the RWF can also be represented as a convolution of the pulse shape $g(s)$ and the indicator function for the range gate $W(s)$:

$$Q_S(r) = \int_{-\infty}^{+\infty} g(r-s)W(s)ds, \quad (16)$$

where the pulse shape directly corresponds to Eq. (5), giving

$$g(s) = \frac{2\sqrt{\ln 2}}{\Delta r \sqrt{\pi}} \exp\left(-4 \ln 2 \frac{s^2}{\Delta r^2}\right), \quad (17)$$

with $\Delta r = c\tau_P/2$, and the indicator function from Eq. (7) transformed to the spatial domain is given by

$$W(s) = \begin{cases} 1/\Delta R, & |s| \leq \Delta R/2, \\ 0, & |s| > \Delta R/2, \end{cases} \quad (18)$$

with the spatial range gate $\Delta R = cT_W/2$ (Robey and Lundquist 2022). Upon computation of Eq. (16), one arrives at the RWF defined by Eq. (8).

3) LLS SPECIFICATIONS

The LLSs in this study aim to model idealized lidars in the style of the Vaisala (formerly Leosphere) WindCube 200S ($\lambda = 1.54 \mu\text{m}$). The Vienna International Airport campaign (Holzäpfel et al. 2021) employed WindCubes at five locations along the glide path. Lidar parameters in Table 2 in front of the semicolon indicate virtual lidars modeling the aforementioned campaign. Virtual lidars after the semicolon aim to generalize the LLS analysis further.

In Vienna, all lidars were placed on the starboard side of the glide path. We additionally position LLSs on the port

TABLE 2. LLS parameters. The x_O^* positions are 26 in total, equidistant in an interval. Each x_O^* is available with all possible y_O^* , where each y_O^* is linked to a specific elevation angle spectrum. Furthermore, LLSs are placed on both sides to the y axis, and values of y_O^* in the table are thus magnitudes only. Half of the LLSs initiate with an RHI scan at φ_- , and the other half of the LLSs initiate with an RHI scan at φ_+ . Note that the origin of the y axis is centered in the LES domain as sketched in Fig. 4.

Parameter	Symbol	Unit	Idealized Vaisala WindCube 200S
Number of lidars	—	—	312
Min/max elevation angle	$[\varphi_-, \varphi_+]$	$^\circ$	$[0, 20], [0, 25], [0, 18], [0, 28], [0, 29]; [0, 20]$
Min/max range gate	$[R_-, R_+]$	m	$[80, 530]; [210, 660]$
x^* -position lidar	x_O^*	—	$[0.0, 17.1]$ with a spacing of 0.67
y^* -position lidar	y_O^*	—	$(5.9, 4.7, 7.2, 5.2, 5.7; 10.0)$
z^* -position lidar	z_O^*	—	0
Temporal range gate	T_W	ns	140
FWHM pulse width	τ_P	ns	200
Angular resolution	$d\varphi$	$^\circ$	0.2
Scanning rate	ω_S	$^\circ \text{ s}^{-1}$	4
Lidar time step	dt'	s	0.05
Range gate spacing	dR	m	3
Sensing volume length	Δz	m	35.6
Midpoint rule interval	$[-\hat{R}, +\hat{R}]$	m	$[-30, 30]$
Aerosol model spacing	h	m	1

side. By mirroring scans from port side LLSs about the glide path axis and swapping starboard and port vortices (assuming mirror symmetry), we obtain LLS scans from the starboard side with both port and starboard crosswinds.

3. Results

a. Numerical wake vortex simulation results

The wake vortex simulations capture all phases of wake vortex evolution in ground proximity well. In the near field, “A” in Fig. 5, the wake behind an aircraft is highly complex—multiple vortices detach from the aircraft geometry. In high-lift configuration, two vortex types dominate in the extended near field (see “B”): the flap-tip and the wing-tip vortices. Figure 5

shows that the flap-tip vortices dominate, until the merging of the two main corotating vortices on each side of the aircraft, resulting in their superposition and a single vortex (see “C”).

High vorticity is visible on the ground as the aircraft reduces its altitude, eventually leading to detaching secondary vortices from the ground (Fig. 6), with positive streamwise vorticity in comparison to negative streamwise vorticity by the primary wake vortices (see red arrow). These secondary vortices then interact with the primary wake vortices (red arrow in Fig. 7), leading to their decay.

Wake vortex trajectories in quiescent atmosphere are plotted in Figs. 8 and 9. The simulation neatly reproduces trends from Stephan et al. (2014). Prior to touchdown ($t_L^* < 0$), the roll up process of the vortices is captured, and vortex circulation

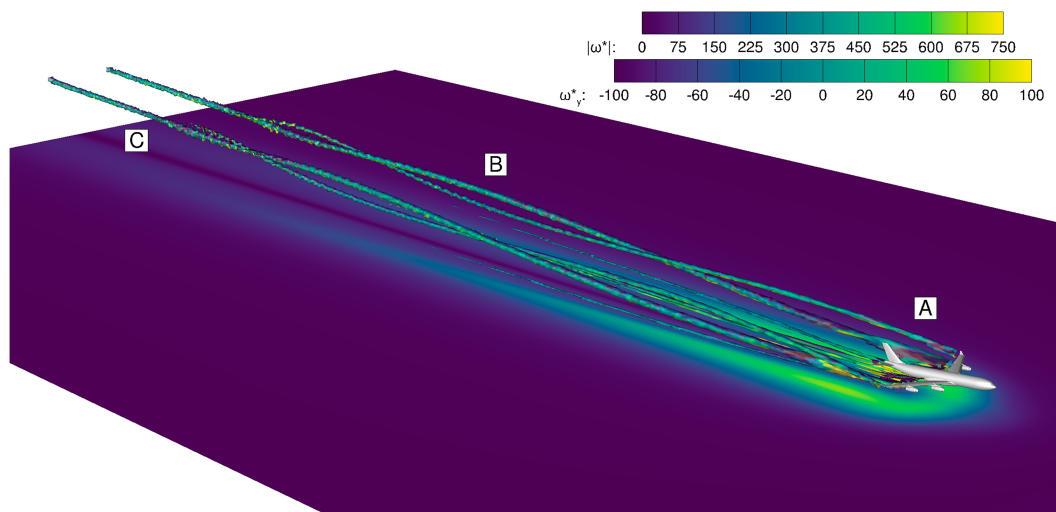


FIG. 5. Airbus A340 landing at $t_L^* = -0.03$ and altitude $z^* = 0.05$ in quiescent atmosphere. The ground is colored by the overall vorticity magnitude $|\omega^*|$. The shown isosurface is $|\omega^*| = 300$ while being colored by the spanwise vorticity ω_y^* to make vortex deformations apparent.

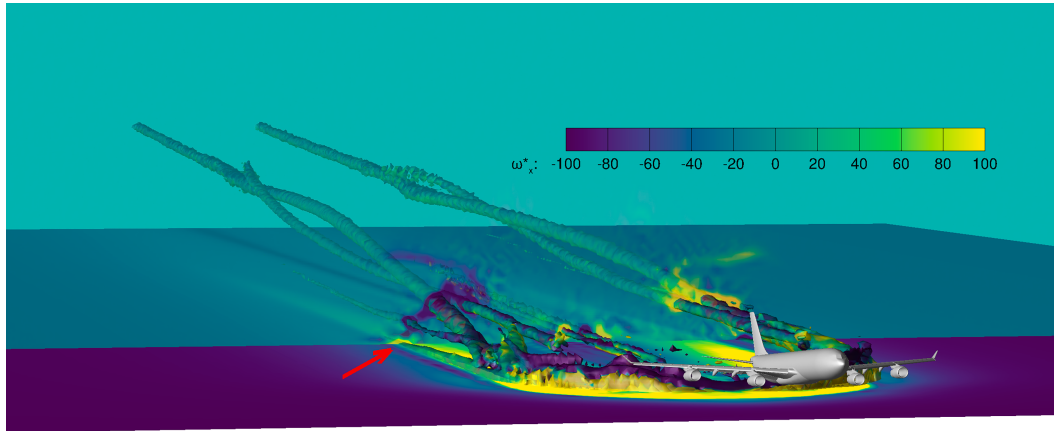


FIG. 6. Detaching secondary vortices from the ground at $t_L^* = 0.02$ in quiescent atmosphere. The vertical slice is colored by the streamwise vorticity ω_x^* , and all other settings are analogous to Fig. 5.

is characterized significantly below Γ_0 . At $t_{L,0}^*$, given by the blue lines in the lower plot of Fig. 9, the circulation is below Γ_0 far away from the touchdown point ($x^* = 16.5$) and steadily increases toward the touchdown point. Circulations of above Γ_0 can be reached in near ground proximity pointing to the wing in ground effect (Stephan et al. 2014). In this paper, vortices are not tracked until the touchdown point; however, Stephan et al. (2014) show a dramatic drop in circulation in this region. With time furthering, the vortex strength decreases, even though rebounds of vortices, as seen in the center plots of Figs. 8 and 9, can lead to temporary strength increases. Gerz et al. (2002) and Holzäpfel and Steen (2007) split aircraft wake vortex decay into two phases: first, a slow diffusion phase, followed by a rapid decay phase. Probably due to the interaction of flap- and wing-tip vortices and the complex three-dimensional dynamics in ground proximity, this distinct two-phase decay is not so clearly discernible in the current LES.

Limitations of the numerical simulations and the associated vortex analysis are twofold. First, the fluctuation of strength and position tends to increase with time, for instance, consider

the $t_L^* = 3$ case in Fig. 9. Due to ground and end effects (Bao and Vollmers 2005; Moet et al. 2005), a pressure difference within the center of the vortex causes axial flow and disturbances (Stephan et al. 2014), so that vortices have a fluctuating motion and are rarely coaxial with the x axis. This limits the truthful vortex tracking and thus the ground truth. Second, vortices tracked particularly close to the lateral boundaries may be unphysical. Consider the pink, i.e., $x^* = 12$, case in Fig. 8; at $t_L^* \approx 4$, the vortices come very close to the side boundaries. With periodic side boundary conditions, the vortices are subject to their counterpart in the imaginary part of the computational domain. We see an almost constant lateral position while inducing upward velocity onto each other (opposite of the usual wake vortex pair) and therefore rising in altitude. Simulated LLS scans subject to behavior as described above are rejected for the analysis.

Similar trends hold for the simulated crosswind aircraft landings (see Figs. 10 and 11). With an increase in crosswind strength, the asymmetry between the counterrotating vortices becomes more prominent. It was expected that a crosswind

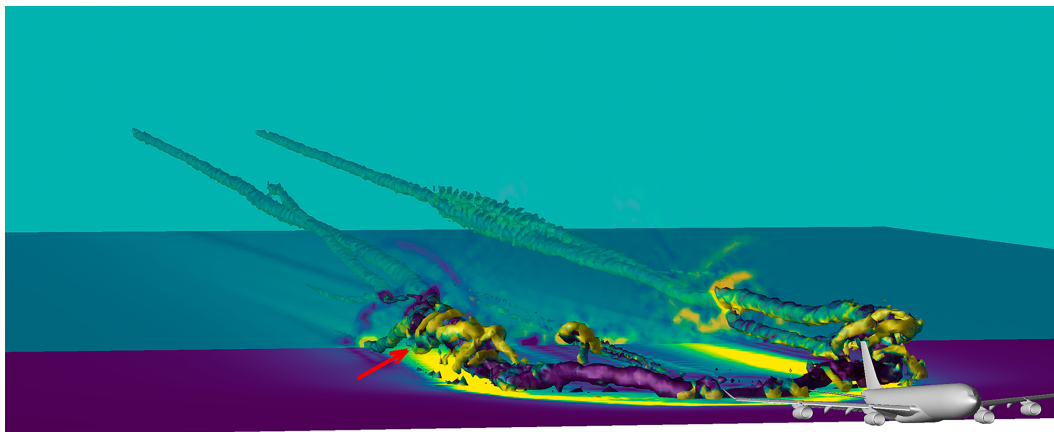


FIG. 7. Interacting secondary vortices and wake vortices at $t_L^* = 0.05$ in quiescent atmosphere. All settings are analogous to Fig. 6.

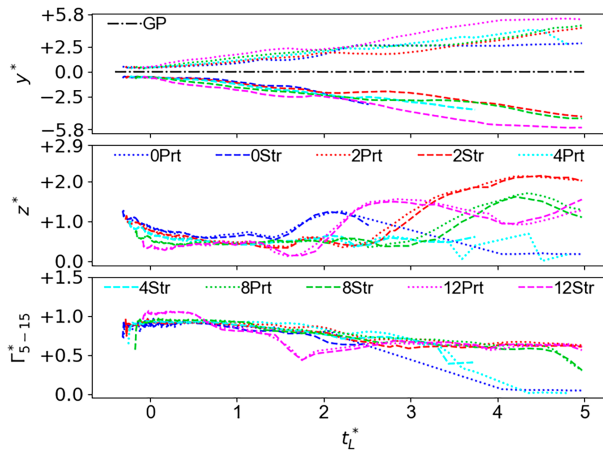


FIG. 8. Temporal Str and Prt vortex development, in terms of circulation Γ_{5-15}^* , lateral position y^* , and distance above the ground z^* (in the numerical simulation coordinate system), in quiescent atmosphere for five x^* positions, multiples of b_0 (see legend). Plot limits are chosen according to the size of the computational domain. The GP of the aircraft is located at $y^* = 0$. Asynchronous termination of vortex tracking may arise when the tracking of a vortex has failed.

strength of $0.5 w_0$ halts the lateral movement of the luff vortex; however, due to descend of the aircraft and the logarithmic boundary layer, only at an altitude of b_0 , this condition can be expected. As the altitude plot of Fig. 10a shows, most wake vortices (with the exception of later rebound) are located below b_0 , thus experiencing lower crosswind speeds and higher mutual velocity induction with the vorticity layer establishing at the ground surface. Nonetheless, the blue case, i.e., vortices at $x^* = 0$ are closest to an altitude of b_0 , and as the y^* plot of Fig. 10a proves, the luff vortex holds its lateral position until $t^* \approx 2.5$, after which additional effects lead to a slow outward transport. Regardless of minor crosswind deviations, the strength of the secondary vortices on the luff vortex side should be weaker than the strength of the lee secondary vortices. The bottom plots of Figs. 10a and 11a show the luff vortex exhibiting a higher circulation in most regions. Overall, observations from Holzäpfel et al. (2016) are agreed with, even if their initialization of a vortex pair expectedly delivers far less noisy results.

The vortex-induced lateral propagation speed is matched more frequently when the crosswind strength of $1.0 w_0$ is set at the altitude of b_0 . In the y^* plots of Figs. 10b and 11b, only toward t_L^* and spatially close to the touchdown point, the discernible lateral movement of the port vortex is visible. By comparing the circulation plots of Fig. 11, we notice that with an increase in crosswind strength, the difficulties to track the vortices also increase. At a crosswind strength of $2.0 w_0$, vortices are laterally transported well over b_0 from the glide path within less than t_0 (except in explicit ground vicinity). Lateral transport of 50 m ($\approx b_0$) is often a threshold beyond which vortices are no longer considered a threat (Gurke and Lafferton 1997; Holzäpfel et al. 2021). Furthermore, comparison of the

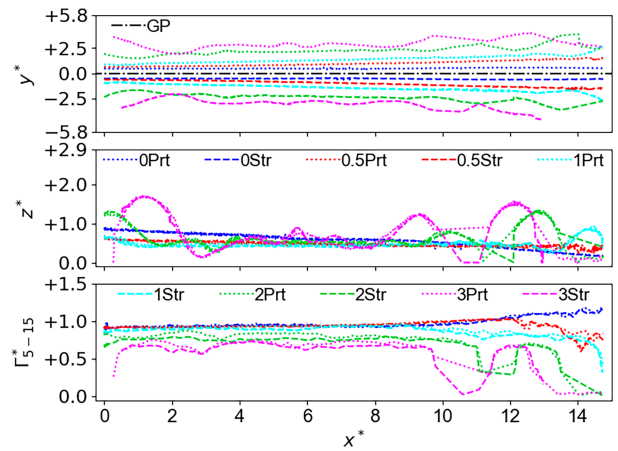


FIG. 9. Longitudinal Str and Prt vortex development, in terms of circulation Γ_{5-15}^* , lateral position y^* , and distance above the ground z^* (in the numerical simulation coordinate system), in quiescent atmosphere for five t_L^* values, multiples of t_0 (see legend). Plot limits are chosen according to the size of the computational domain. The GP of the aircraft is located at $y^* = 0$. Asynchronous termination of vortex tracking may arise when the tracking of a vortex has failed.

circulation plots of Fig. 11 highlights far earlier strength reduction of vortices along the entire glide path. The earlier loss of coherency and the thereby decay is also a result of the increased turbulence in the atmosphere as the crosswind strength increases.

b. LLS results

Virtual lidar measurements within the wake vortex simulations are subject to typical lidar measurement restrictions: 1) the smearing out of the flow in the atmosphere due to the RWF, 2) the temporal delay in recording an RHI scan, and 3) the RHI lidar scan geometry. For investigating the impact of the RWF, we assume that point measurements are possible and solely compute Eq. (14) at the desired range gate centers along the LOS, without the application of the RWF shown in Fig. 12 (right). Four exemplary LLS scans, produced in challenging scenarios, are given in Fig. 12 (left), where the RWF has been applied. As expected, we observe high velocities and steep gradients being filtered out by the RWF scans; scans without the RWF feature at least one further velocity layer. On top of this, a smearing out of the velocity field results, leading to an increased vortex core. Both effects may have an effect on the vortex strength evaluation.

Vortices close to the ground appear to have a strong increase in velocity in their lower half compared to their upper half. Axisymmetric vortices are typically expected; however, the ground represents a wall along which secondary vorticity is produced. The effect of this vorticity can be modeled and understood with the concept of imaginary mirror vortices of opposite vorticity below the computational domain that interacts with the flow field. Their presence is confirmed by vertical velocity contours of the velocity layers close to the ground. So, the vortex half closer to the ground is strengthened, while the upper vortex-half is attenuated. With no RWF applied,

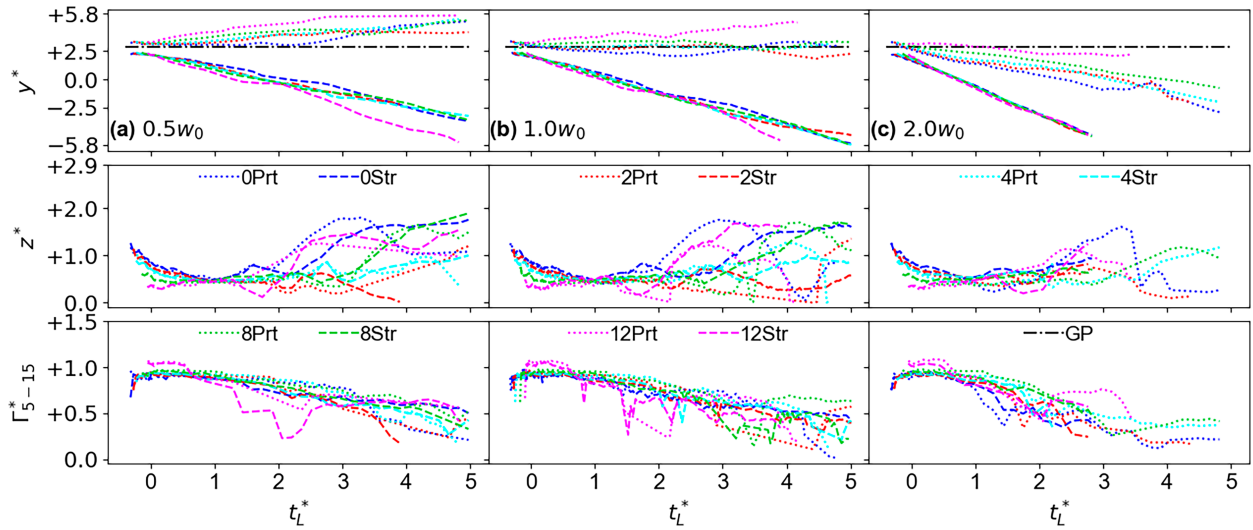


FIG. 10. Temporal Str and Prt vortex development, in terms of circulation Γ_{5-15}^* , lateral position y^* , and distance above the ground z^* (in the numerical simulation coordinate system), under various Prt crosswind strengths (one per column) for five x^* positions, multiples of b_0 (see legend). Plot limits are chosen according to the size of the computational domain. The GP of the aircraft is located at $y^* = 2.8$. Asynchronous termination of vortex tracking may arise when the tracking of a vortex has failed.

lidar scans also contain far more detail and secondary vortices in comparison to LLS scans, where differentiating between wing-tip and flap-tip vortices is not possible. Even before the merging of corotating vortices, we must regard the vortices as a whole overlapping vortex.

Since RHI lidar scans are made up of multiple LOSs, a time delay of several seconds exists within each scan. Depending on whether the scanning rate ω_S is positive or negative, during the recording of an RHI lidar scan, the elevation angle φ continuously increases $+\varphi \equiv t_{\varphi_-} < t_{\varphi_+}$ or decreases $-\varphi \equiv t_{\varphi_+} < t_{\varphi_-}$. If vortices are generated during the scan recording, as in Fig. 12a,

only one-half of the aircraft wake is visible. Even if the wake is fully represented in an RHI lidar scan, depending on the scanning pattern ($+\varphi$ or $-\varphi$) and the vertical transport of the vortex during the scan recording, vortices can be stretched (Stc) or compressed (Com), which may result in a strength under- or overestimation (Smalikhov 2019).

Another downside of lidar recordings is their scan geometry. It is not always possible to include the entire wake of an aircraft in lidar scans as vortices may advect out of the measurement window. Particularly when vortices are partly visible in the scans, such as in Fig. 12b, lidar characterization algorithms may

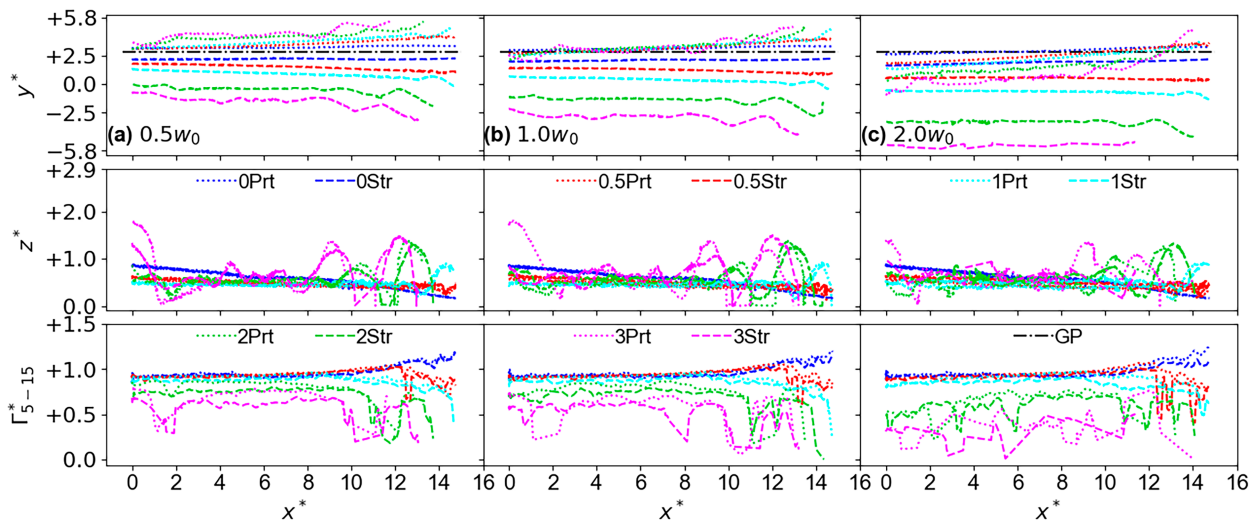


FIG. 11. Longitudinal Str and Prt vortex development, in terms of circulation Γ_{5-15}^* , lateral position y^* , and distance above the ground z^* (in the numerical simulation coordinate system), under various Prt crosswind strengths (one per column) for five t_L^* values, multiples of t_0 (see legend). Plot limits are chosen according to the size of the computational domain. The GP of the aircraft is located at $y^* = 2.8$. Asynchronous termination of vortex tracking may arise when the tracking of a vortex has failed.

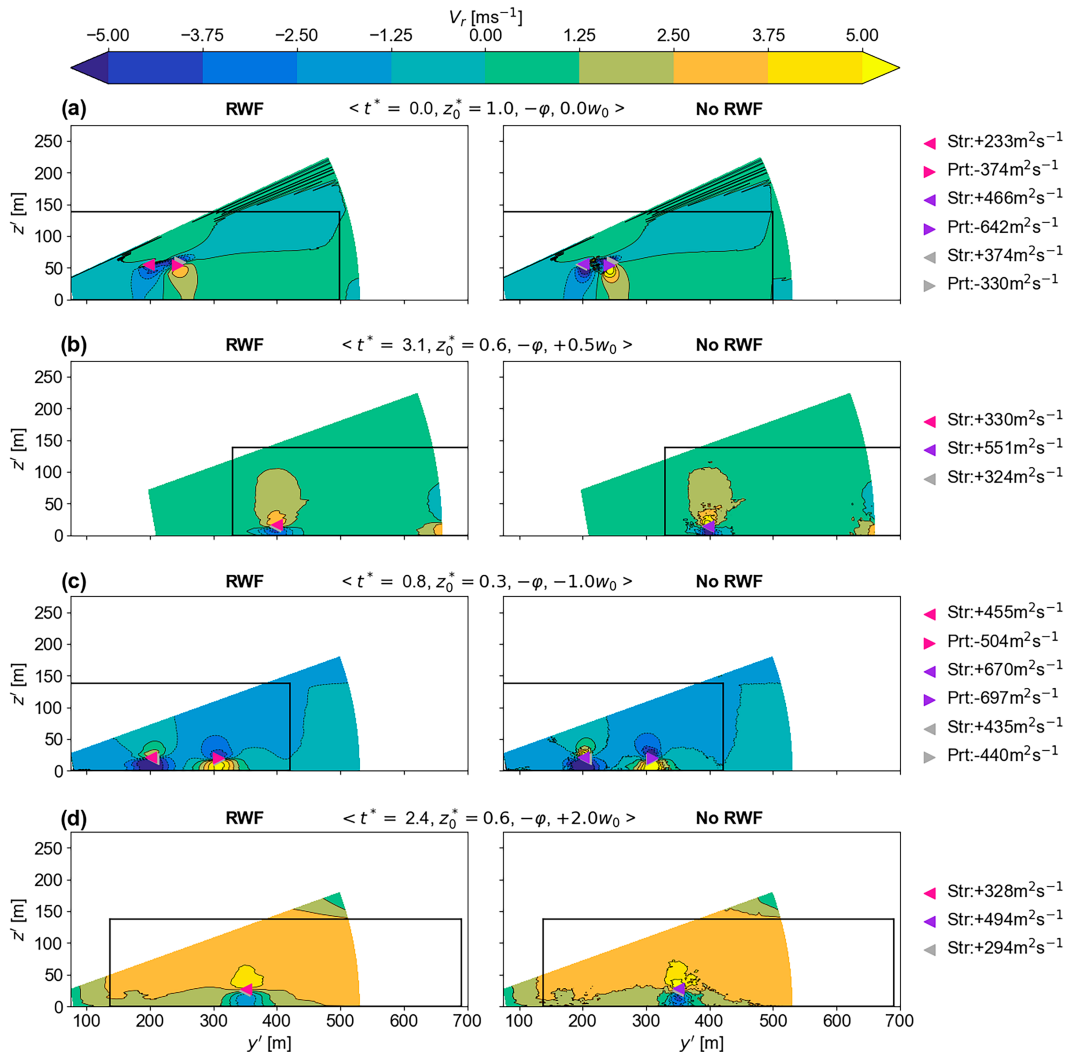


FIG. 12. LLS scans in challenging scenarios (left) with and (right) without RWF applied for various crosswinds and directions. Wake vortex location characterizations (markers) and strength characterizations (see legends) of the ST and the RV method are given. Gray markers represent the ST, which are often overshadowed by the pink and violet markers which arise from the RV method with and without the RWF, respectively. The wake vortex age t^* , the aircraft altitude at passage of the lidar measurement plane z_0^* , the scan sense ($+\varphi$ or $-\varphi$), and the crosswind $\pm\chi w_0$ are given for each case. The black rectangle represents the LES computational domain.

struggle to correctly identify them and strength under- or over-estimations may result.

A limitation exclusive to LLS scans concerns the padding method, which is responsible for velocities outwith the computational domain, the black rectangle. Generally, it extends the flow field without unphysical gradients, for example, in Fig. 12b. However, in few cases, such as Figs. 12a and 12c, gradients are excessively extended from within the computational domain. In other cases, new velocity gradients emerge due to padding being performed in the Cartesian coordinate system. For instance, Fig. 12d introduces new gradients in the padding region, caused by velocities outwith the computational domain targeted to approach zero. The padding is most suitable for a quiescent atmosphere in comparison to a crosswind case.

Minimal impact on the success of wake vortex characterization is expected, as they are rarely located in the vicinity of the padded scan areas.

c. RV method assessment

1) DATASET

A subset of obtained LLS scans is characterized by the RV method for its evaluation. Selecting a representative subset follows two steps. First, an accurate ground truth is computed via the pressure–vorticity algorithm from section 2b. By implementing both quantitative and qualitative checks, primarily relying on following the vortex trajectories and strength trends, a carefully curated dataset is obtained. Quantitative

TABLE 3. Dataset split by crosswind strength χw_0 and wake vortex type.

Crosswind	No. of Prt vortices	No. of Str vortices	No. of LLS scans
$0.0w_0$	528	427	531
$0.5w_0$	510	447	557
$1.0w_0$	543	503	676
$2.0w_0$	298	268	378
Total	1879	1645	2142

checks include circulation sense, strength drop, and extreme strength as well as vortex position. Nonetheless, outliers cannot be ruled out completely, only minimized, due to the turbulent nature of the flow. The subset is given in Table 3. Cases where the RV method fails completely occur when vortex centers are too close to the edges of the scan, or when vortices possess minimal coherency. The latter leads to the lower number of LLS scans measured in the $2.0w_0$ crosswind strength simulation.

2) QUANTITATIVE ACCURACY

The characterization accuracy of the investigated RV method version is given in Table 4. The medians of the error values (omitting outliers) of the polar coordinates to a vortex center E_{φ_C} and E_{R_C} , as well as the normalized two-norm for the Cartesian coordinates to the vortex center $D_C^{\text{med,*}}$, and the vortex circulation $E_{\Gamma_{5-15}^*}$ are given. No significant difference in characterization accuracy is observed for the port and starboard vortices, likely thanks to LLS scans with both crosswind directions. There is no universally accepted circulation below which wake vortices are no longer considered hazardous, yet vortices with $\Gamma_{5-15} < 25 \text{ m}^2 \text{ s}^{-1}$ ($\Gamma_{5-15}^* < 0.06$) are certainly below relevance for fixed wing aircraft. This may differ for helicopters and other UAM vehicles. Although the medians of the error values in Table 4 are small, the standard deviations (Stds) of the errors reveal a significant spread in accuracy (see Fig. 13) and should be included when quoting the RV method accuracy. Therefore, the total RV method circulation characterization accuracy should be reported as ranging from -13.9 to $+52.3 \text{ m}^2 \text{ s}^{-1}$, where the median circulation error is $19.2 \text{ m}^2 \text{ s}^{-1}$ and the bounds arise from the standard deviation ($33.1 \text{ m}^2 \text{ s}^{-1}$). A negative/positive error refers to an under-/overestimation by the RV method. In most cases, the vortex strength is overestimated. The median localization accuracy is close to $dR = 3 \text{ m}$, i.e., the spacing

of range gates along a LOS. It is questionable whether undercutting the lidar measurement accuracy is possible. Also as the spread in localization error is large, the standard deviation elevates to nearly twice the measurement accuracy (5.7 m). While the circulation error distribution can be described as Gaussian, the distribution of D_C^* is positively skewed and thus increasing the difference between the mean and median (see Fig. 13).

Errors in the circulation characterization of the RV method are twofold. An inaccurate vortex localization significantly disrupts an accurate circulation characterization, which itself has multiple sources of error. Combining this leads to a systematic error drawn in Fig. 14 in the full range of circulation magnitude. Unsurprisingly, the error spread is higher for weak vortices as their coherency is lower if generated by the same aircraft type.

In Table 5, the RV method accuracy is given for increasing turbulent crosswind strengths. A significant detriment in accuracy occurs with a crosswind strength of $2.0w_0$, and both the median accuracy and its standard deviation increase. If we define a circulation characterization accuracy range as above, for the $2.0w_0$ crosswind case, a vortex circulation uncertainty ranging from -15.3 to $+68.2 \text{ m}^2 \text{ s}^{-1}$ must be considered.

Table 6 splits the vortex characterizations by luff and lee vortices for the LLS scans performed under crosswind conditions. Only a marginal difference is found for the vortex strength characterization accuracy; however, the localization error of lee vortices is nearly twice that of the luff vortices. Luff vortices are expected to be coherent for longer periods of time; thus, already at younger vortex age, the characterization of lee vortices is more challenging. At the same vortex age, lee vortices are also weaker; hence, the impact of this discrepancy is not hugely consequential for operational purposes.

To this day, only theoretical accuracy estimations by Smalikho et al. (2015) and numerical experiments by Smalikho (2019) have existed for rating the RV method. Both these investigations do not account for the complex flow behind an aircraft, employ vortex models, and assume a quiescent atmosphere. Table 7 compares these theoretical RMS error (RMSE) values for the elevation angle to the vortex center φ_C , the range to the vortex center R_C , and the vortex strength Γ_{5-15} to the RMSE values from our study. In practice, one can expect RMSE values of just over triple the theoretical RMSE (without considering the error spread). Primary reasons for the underestimation of the error by Smalikho et al. (2015) and Smalikho (2019) can be associated with the lack of both incoherence and

TABLE 4. The medians of the error values E of the polar coordinates for defining a vortex center position (R_C , φ_C), the circulation Γ_{5-15}^* , and the medians of the two-norm error values for the vortex center D_C^* (in the Cartesian coordinate system). The \pm represent an over- and underestimation by the RV method in comparison to the ground truth, respectively. The spread of the error is given by the Std. The normalizations for D_C^{med} and $E_{\Gamma_{5-15}^*}$ are performed via $b_0 = 47.4 \text{ m}$ and $\Gamma_0 = 433.9 \text{ m}^2 \text{ s}^{-1}$, respectively.

Vortex type	E_{φ_C} (°)	E_{R_C} (m)	$D_C^{\text{med,*}}$ (-)	$E_{\Gamma_{5-15}^*}$ (-)
Str	$+0.47 \pm 0.54$	-0.71 ± 3.95	0.06 ± 0.06	$+0.05 \pm 0.08$
Prt	$+0.36 \pm 0.37$	$+0.06 \pm 4.57$	0.07 ± 0.06	$+0.04 \pm 0.07$
Total	$+0.41 \pm 0.46$	-0.31 ± 4.32	0.06 ± 0.06	$+0.04 \pm 0.08$

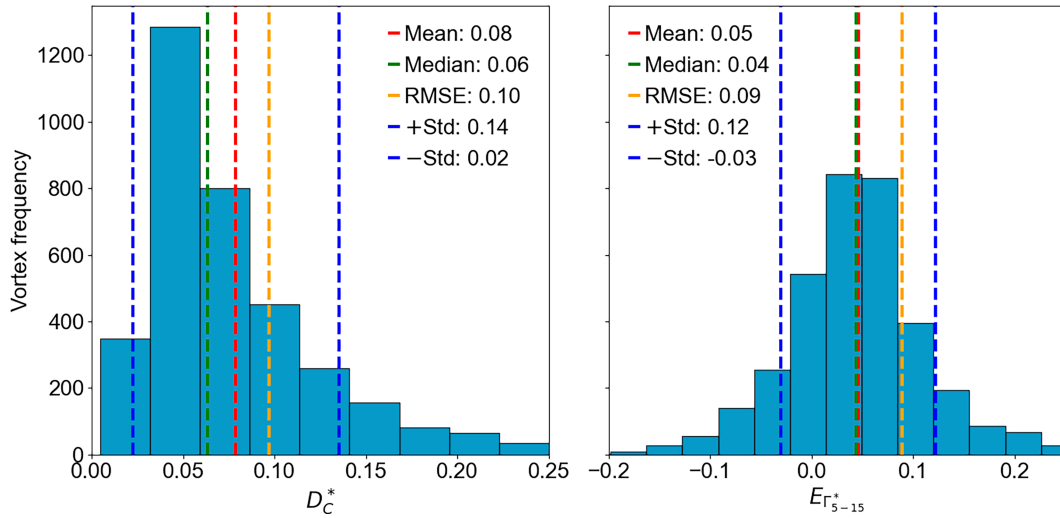


FIG. 13. Two-norm error for the vortex center (left) D_C^* and (right) $E_{\Gamma_{5-15}^*}$ with respect to their frequency in the dataset. The mean, median, RMSE, and the Std from the mean are plotted (with the respective error values) for the two cases. Bins with few vortices (belonging to higher errors) are not shown.

unambiguousness of vortices analyzed, in comparison to field measurements.

3) DISCUSSION

Returning to the spatial averaging caused by the RWF as discussed in section 3b. The legends of Fig. 12 as well as markers within the lidar scans allow a second look at the LLS scans in comparison to simulated lidar scans without the RWF applied. The ground truth is given by gray markers. The pink

and violet markers give the RV method estimations with and without the RWF applied, respectively. Note that the model function \tilde{V}_r in Eq. (10) does not take into account the RWF. In comparison to the ground truth, the RV method overestimates the vortex strength, with a dramatic overestimation when the RWF is not applied. Particularly, vortices located close to the edges of the scan geometry are subject to larger characterization errors (see Fig. 15). The ground truth is not restricted to the lidar geometry and sees the vortices as a whole, unlike the RV algorithm.

Vortices at low altitudes are subject to larger inaccuracies. Similar observations have been made in field measurements (F. Holzäpfel 2024, personal communication). The vortex altitude with respect to the circulation error is plotted in Fig. 16. In section 3b, the presence and effect of mirror vortices were discussed. The strength of vortices close to the ground is overestimated as a result. Depending on the method for computing the vortex circulation, the impact on the estimate differs. Equation (1) showed two ways for computing the vortex circulation, either via the vorticity or via the tangential velocity along a line (other methods exist, but these play no role in this paper) (Holzäpfel et al. 2003). The ground truth

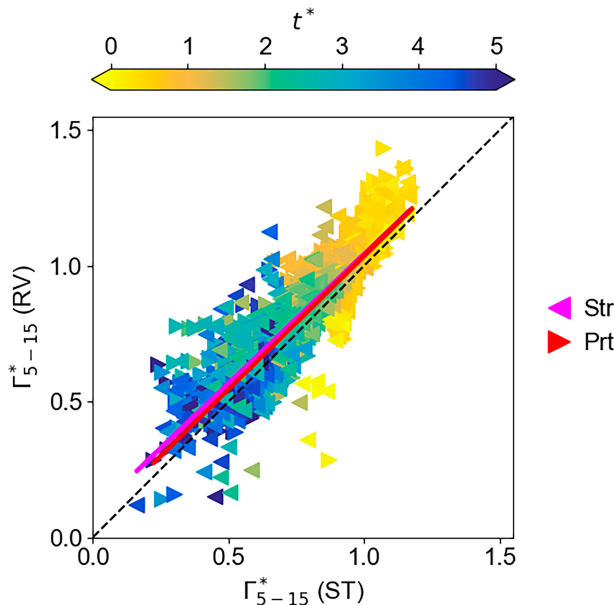


FIG. 14. Correlation of the circulation Γ_{5-15}^* estimated by the RV method and ST. Estimates are divided into Str and Prt vortex groups. Wake vortex characterizations (markers) are colored by the vortex age.

TABLE 5. The medians of the error values for the circulation $E_{\Gamma_{5-15}^*}$ and the medians of the two-norm error values for the vortex center $D_C^{med,*}$ (in the Cartesian coordinate system) split by crosswind strength χw_0 . The \pm represent an over- and underestimation by the RV method in comparison to the ground truth, respectively. The spread of the error is given by the Std.

Crosswind	$D_C^{med,*}$ (-)	$E_{\Gamma_{5-15}^*}$ (-)
$0.0w_0$	0.06 ± 0.04	$+0.04 \pm 0.07$
$0.5w_0$	0.06 ± 0.05	$+0.04 \pm 0.07$
$1.0w_0$	0.06 ± 0.06	$+0.04 \pm 0.07$
$2.0w_0$	0.08 ± 0.07	$+0.06 \pm 0.10$

TABLE 6. The medians of the error values for the circulation $E_{\Gamma_{5-15}^*}$ and the medians of the two-norm error values for the vortex center $D_C^{\text{med},*}$ (in the Cartesian coordinate system) for LLS scans under crosswind, separated by vortex position with respect to the wind direction (luff/lee). The \pm represent an over- and underestimation by the RV method in comparison to the ground truth, respectively. The spread of the error is given by the Std.

Vortex	$D_C^{\text{med},*}$ (-)	$E_{\Gamma_{5-15}^*}$ (-)
Luff	0.05 ± 0.06	0.05 ± 0.08
Lee	0.09 ± 0.06	0.04 ± 0.07

algorithm makes use of the vorticity. Instead, the RV method fits Burnham–Hallock vortex models via few tangential velocities to the primary vortex pair in Eq. (10). No mirror vortices are considered by this RV method version. It assumes the superposed velocities only result from the primary vortices, and thus, their strengths are overestimated. Moreover, when the vorticity is employed for circulation computation, it allows the vortex to be incoherent. The RV method assumes axisymmetric coherent vortices and, therefore, interprets the additional velocity from the mirror vortices as genuine primary vortices. Note that the free-slip boundary at the top of the computational domain can also be modeled by mirror vortices (Doligalski et al. 1994), and an analogous physical mechanism can be expected in the simulation. In reality, such effects would not exist. With a computational domain height of $2.9b_0$, the minimum error is expected in the vertical center at $1.45b_0$ —and indeed at this altitude, the vortex circulation is just not overestimated on average (see Fig. 16). Figure 11 in Holzäpfel et al. (2021) reports a vortex strength underestimation on the order of 10% in field measurements instead. Potentially even at the vertical center of our computational domain, mirror vortices still impact the strength estimation, overshadowing the inherent underestimation of the method [the field measurements by Holzäpfel et al. (2021) generally feature vortices at higher altitudes, reducing the mirror vortex effect]. With regards to Fig. 16, for $1.5 \lesssim z^*$, the upper boundary seemingly begins to influence the characterization by the RV method; however, the lidar geometry also plays a role here (recall Fig. 15). The strength of strong and coherent vortices located within $0.5 \lesssim z^* \lesssim 1.0$ is often underestimated by the RV method. Given that the wake vortex simulations result in a high number of strong vortices at low altitude, it is likely that the negligence of mirror vortices by this RV method version is the main driver for

TABLE 7. LLS-based and theoretical [by Smalikho et al. (2015), Smalikho (2019)] RMSE values of the polar coordinates for defining a vortex center position (R_C , φ_C), the circulation Γ , and the RMSE of the two-norm error for the vortex center D_C^{RMSE} (in the Cartesian coordinate system). The spread of the error is given by the Std. RMSE_Γ for the LLS is assumed equivalent to $\text{RMSE}_{\Gamma_{5-15}}$ for this comparison. The theoretical RMSE_{φ_C} , RMSE_{R_C} , and lower bound RMSE_Γ originate from Smalikho et al. (2015) for a SNR of 0.05. Theoretical D_C^{RMSE} and the upper bound of RMSE_Γ originate from Smalikho (2019), considering $+\varphi$ and no instrument noise. Theoretical RMSE values for higher SNR values, thus more favorable measurement conditions, were computed by Smalikho et al. (2015). Note the difference of the given RMSE values in comparison to the medians of the error values in the “total” case from Table 4.

Error type	RMSE_{φ_C} (°)	RMSE_{R_C} (m)	D_C^{RMSE} (m)	RMSE_Γ ($\text{m}^2 \text{s}^{-1}$)
LLS	0.63 ± 0.46	4.3 ± 4.4	4.6 ± 2.7	38.7 ± 33.1
Theoretical	0.21	1.8	1.0	10.3–21.0

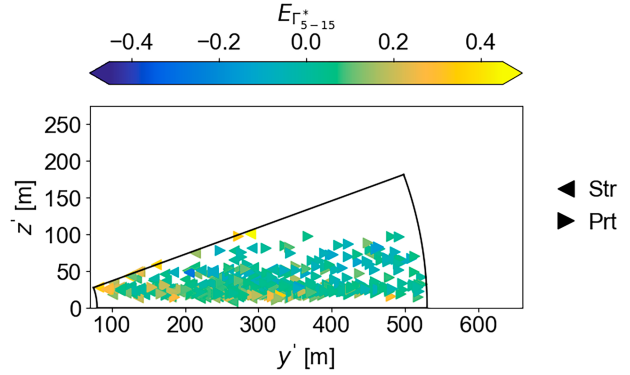


FIG. 15. Sample LLS scan geometry of $[R_-, R_+] = [80, 530]$ and $[\varphi_-, \varphi_+] = [0, 20]$ with vortex characterization. Estimates are divided into Str and Prt vortex groups. Markers of individual wake vortex characterizations are colored by the error between the RV method and the ground truth. The \pm represent an over- and underestimation by the RV method in comparison to the ground truth, respectively.

the overall computed strength overestimation. An updated version of the RV method including two mirror vortices has been presented by Smalikho (2019), and the circulation error is approximately halved in their theoretical study.

In section 3b, vortex stretching and compression was discussed in relation to the vortex movement and the lidar scanning rate. A representative number of vortex characterizations are plotted in Fig. 17, comparing the simulation truth and RV method. The impact of vortex stretching and compressing appears minimal. Still, the strength overestimation of stretched vortices appears more pronounced, confirming the idealized study for strong vortex descend by Smalikho (2019).

An additional limitation of the RV method concerns the requirement of setting a core radius for the Burnham–Hallock vortex model being fit to the vortices. A fixed core radius of 2 m is allocated for wake vortices generated by the A340 aircraft, whereas throughout the lifetime of a wake vortex, its core size may vary substantially. When the core radius is larger or smaller than 2 m, an underestimation or overestimation of the vortex circulation may result.

The localization accuracy of the RV method can be considered satisfactory for tasks such as a ground-based warning system, with the standard deviation of the error constituting the primary downside. The circulation characterization accuracy

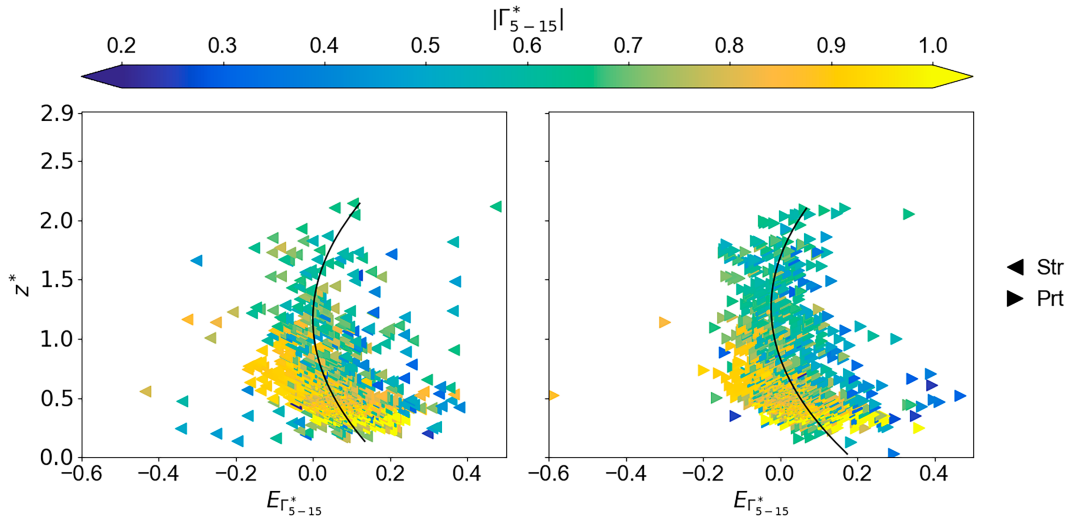


FIG. 16. Circulation error $E_{\Gamma_{5-15}^*}$ against vortex altitude z^* . The z^* axis is limited by the computational domain height. Individual data points are colored by the ground truth normalized circulation magnitude $|\Gamma_{5-15}^*|$. Estimates are divided into (left) Str and (right) Prt vortex groups, and for each, a second-order polynomial is fitted to the data in black.

is more critical, with a characterization window of $66.2 \text{ m}^2 \text{ s}^{-1}$ (two standard deviations). The narrower error spread in Fig. 14 implies that young and strong vortices are characterized with an error close to the medians of the error values presented in Table 4. Thus, the accuracy of the analyzed RV method is, particularly at high vortex altitudes, a satisfactory algorithm for characterizing wake vortices.

4. Conclusions

A new method of assessing the accuracy of wake vortex characterization methods based on lidar measurements has been developed. High-fidelity simulations of the wake vortices generated by a landing Airbus A340 aircraft have been performed under various turbulent crosswind strengths relevant for airport operations. These allow the study of wake vortices from their generation until decay, while their position and strength are known throughout via methods unavailable for field measurements. Virtually installed lidars, so-called LES lidar simulators (LLSs), realistically model the lidar operating, with the primary focus on the volume averaging performed for obtaining line-of-sight (LOS) velocities. A range gate weighting function (RWF) based on the pulse shape and range gate pattern has shown to provide realistic LOS velocities of range-height indicator lidar scans. In general, lidars mollify high velocities and steep gradients due to the convolution with the RWF.

With the aid of a wide range of LLS scans and the available knowledge of the vortices within, we are able to evaluate characterization algorithms for lidar scans used in field measurements. Here, the radial velocity (RV) method, a state-of-the-art wake vortex characterization algorithm for lidar scans, was evaluated. To date, only theoretical accuracy estimates and an experimental numerical extension were available. Particularly under turbulent atmospheric conditions, the performance was unknown. It was found that the overall RMSE values are approximately three times higher than those estimated with analytical means (Smalikho et al. 2015; Smalikho 2019). The medians of the error values for both the position and strength characterization can be considered small for most applications, and the localization of vortices is within instrument accuracy. However, the error spread unveils a high

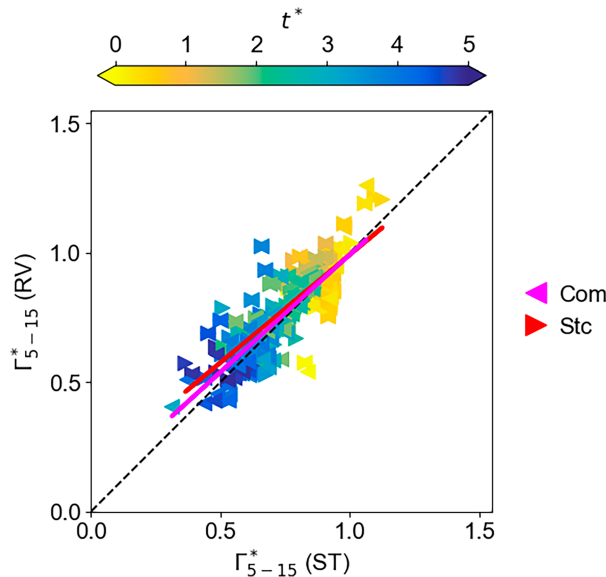


FIG. 17. Correlation of the circulation Γ_{5-15}^* estimated by the RV method and ST. Estimates are divided into Stc and Com vortex groups. Wake vortex characterizations (markers) are colored by the vortex age and limited to the wake vortex simulation with no wind present.

uncertainty in the characterizations. Particularly under highly turbulent conditions, the RV method struggles to provide a narrow error bound. Careful segmentation of the results allows distinguishing several origins of the errors. These arise from simulation assumptions, lidar operation aspects, but crucially also the RV method itself. Most notably, the investigated RV method version does not consider mirror vortices when characterizing the strength of vortices in LLS scans in ground proximity. At altitudes superseding one initial vortex separation above ground, the systematic error of strength characterization by the RV method appears very low. However, serious vortex strength overestimation exists for vortices near the ground. Overall, an overestimation in vortex strength is found; given that most vortices in this study are close to the ground, the impact of the lack of mirror vortices seems critical for the RV method.

Future studies can greatly benefit from the variety in wake vortex simulations and LLSs placed in the LES, providing an extensive and labeled dataset of high-fidelity simulated lidar scans. We aim to evaluate further lidar characterization methods with this dataset, allowing more reliable judgment of past and also future studies involving lidar measurements. The availability of this labeled dataset is also a valuable asset for machine learning (ML). Training ML models with LLS scans has the potential to process wake vortex lidar data both in real time and with an accuracy exceeding traditional processing algorithms as the RV method. This in turn may advance the development and implementation of systems to safely decrease aircraft separations in the terminal environment.

Acknowledgments. Funding was received from the German Federal Ministry for Digital and Transport within the mFUND project “KIWI” and from the German Aerospace Center (DLR) undertaking “Wetter und Disruptive Ereignisse.” We thank DLR’s Institute of Aerodynamics and Flow Technology for providing the results of the RANS simulations from the EU-funded AWIATOR project and Airbus for the allowance to use them. Furthermore, we appreciate the kind provision of the original MGLET code by the Technical University of Munich, Hydromechanics. Finally, the authors gratefully acknowledge the Gauss Centre for Supercomputing e.V. (www.gauss-centre.eu) for funding this project by providing computing time on the GCS Supercomputer SuperMUC-NG at the Leibniz Supercomputing Centre (www.lrz.de). The authors declare that they have no conflicts of interest.

Data availability statement. The generated LES lidar simulator dataset can be found via [Wartha et al. \(2024\)](#).

REFERENCES

- Banakh, V. A., and I. N. Smalikho, 1997: Estimation of the turbulence energy dissipation rate from the pulsed Doppler lidar data. *Atmos. Oceanic Opt.*, **10**, 957–965.
- , and —, 2013: *Coherent Doppler Wind Lidars in a Turbulent Atmosphere*. Artech House, 277 pp.
- Bao, F., and H. Vollmers, 2005: Alleviation of end-effect in facilities for far wake investigations. *43rd AIAA Aerospace Sciences Meeting and Exhibit*, Reno, NV, AIAA, AIAA 2005-907, <https://doi.org/10.2514/6.2005-907>.
- BarbareSCO, F., and Coauthors, 2015: Monitoring wind, turbulence and aircraft wake vortices by high resolution radar and lidar remote sensors in all weather conditions. URSI France Journées Scientifiques, 81–110.
- Baumert, H. Z., 2013: Universal equations and constants of turbulent motion. *Phys. Scr.*, **2013**, 014001, <https://doi.org/10.1088/0031-8949/2013/T155/014001>.
- Breitsamter, C., 2007: *Nachlaufwirbelsystem großer Transportflugzeuge – Experimentelle Charakterisierung und Beeinflussung*. Herbert Utz Verlag, 266 pp.
- Burnham, D. C., and J. N. Hallock, 1982: Chicago monostatic acoustic vortex sensing system. Federal Aviation Administration Tech. Rep. DOT-TSC-FAA-79-103.IV, 210 pp., <https://rosap.ntl.bts.gov/view/dot/9391>.
- Critchley, J., and P. Foot, 1991: UK CAA wake vortex database: Analysis of incidents reported between 1982 and 1990. Civil Aviation Authority Tech. Rep. CAA Paper 91015, 23 pp.
- De Visscher, I., F. Rooseleer, and R. Graham, 2020: Time-based separation (TBS) principles as alternative to static distance based separation for final approach. EUROCONTROL Tech. Rep., 80 pp., <https://www.eurocontrol.int/publication/eurocontrol-guidelines-time-based-separation-tbs-final-approach>.
- Doligalski, T. L., C. R. Smith, and J. D. A. Walker, 1994: Vortex interactions with walls. *Annu. Rev. Fluid Mech.*, **26**, 573–616, <https://doi.org/10.1146/annurev.fl.26.010194.003041>.
- EUROCONTROL, 2022: Aviation outlook 2050. EUROCONTROL Tech. Rep. STATFOR Doc 683, 24 pp., <https://www.eurocontrol.int/sites/default/files/2022-04/eurocontrol-aviation-outlook-2050-report.pdf>.
- Frehlich, R., 1997: Effects of wind turbulence on coherent Doppler lidar performance. *J. Atmos. Oceanic Technol.*, **14**, 54–75, [https://doi.org/10.1175/1520-0426\(1997\)014<0054:EOWTOC>2.0.CO;2](https://doi.org/10.1175/1520-0426(1997)014<0054:EOWTOC>2.0.CO;2).
- , and R. Sharman, 2005: Maximum likelihood estimates of vortex parameters from simulated coherent Doppler lidar data. *J. Atmos. Oceanic Technol.*, **22**, 117–130, <https://doi.org/10.1175/JTECH-1695.1>.
- , S. M. Hannon, and S. W. Henderson, 1997: Coherent Doppler lidar measurements of winds in the weak signal regime. *Appl. Opt.*, **36**, 3491–3499, <https://doi.org/10.1364/AO.36.003491>.
- , Y. Meillier, M. L. Jensen, B. Balsley, and R. Sharman, 2006: Measurements of boundary layer profiles in an urban environment. *J. Appl. Meteor. Climatol.*, **45**, 821–837, <https://doi.org/10.1175/JAM2368.1>.
- Gao, H., J. Li, P. W. Chan, K. K. Hon, and X. Wang, 2018: Parameter-retrieval of dry-air wake vortices with a scanning Doppler lidar. *Opt. Express*, **26**, 16377–16392, <https://doi.org/10.1364/OE.26.016377>.
- , —, —, and —, 2019: Parameter retrieval of aircraft wake vortex based on its max–min distribution of Doppler velocities measured by a Lidar. *J. Eng.*, **2019**, 6852–6855, <https://doi.org/10.1049/joe.2019.0539>.
- Gerz, T., F. Holzäpfel, and D. Darracq, 2002: Commercial aircraft wake vortices. *Prog. Aerosp. Sci.*, **38**, 181–208, [https://doi.org/10.1016/S0376-0421\(02\)00004-0](https://doi.org/10.1016/S0376-0421(02)00004-0).
- Gurke, T., and H. Lafferton, 1997: The development of the wake vortices warning system for Frankfurt airport: Theory and implementation. *Air Traffic Control Quart.*, **5**, 3–29, <https://doi.org/10.2514/atcq.5.1.3>.

- Hallock, J. N., and F. Holzäpfel, 2018: A review of recent wake vortex research for increasing airport capacity. *Prog. Aerosp. Sci.*, **98**, 27–36, <https://doi.org/10.1016/j.paerosci.2018.03.003>.
- Harvey, J. K., and F. J. Perry, 1971: Flowfield produced by trailing vortices in the vicinity of the ground. *AIAA J.*, **9**, 1659–1660, <https://doi.org/10.2514/3.6415>.
- Hennemann, I., 2010: Deformation und Zerfall von Flugzeugwirbelschleppen in turbulenter und stabil geschichteter Atmosphäre. Ph.D. thesis, Technische Universität München, 162 pp., <https://mediatum.ub.tum.de/doc/823304/823304.pdf>.
- Hinton, D. A., and C. R. Tatnall, 1997: A candidate wake vortex strength definition for application to the NSA aircraft vortex spacing system (AVOSS). NASA Tech. Memo. NASA/TM-110343, 36 pp., <https://ntrs.nasa.gov/api/citations/19970031683/downloads/19970031683.pdf>.
- Hokpunna, A., 2009: Compact fourth-order scheme for numerical simulations of Navier-Stokes equations. Ph.D. thesis, Technische Universität München, 144 pp., <https://mediatum.ub.tum.de/doc/813362/file.pdf>.
- , and M. Manhart, 2010: Compact fourth-order finite volume method for numerical solutions of Navier–Stokes equations on staggered grids. *J. Comput. Phys.*, **229**, 7545–7570, <https://doi.org/10.1016/j.jcp.2010.05.042>.
- Holzäpfel, F., and M. Steen, 2007: Aircraft wake-vortex evolution in ground proximity: Analysis and parameterization. *AIAA J.*, **45**, 218–227, <https://doi.org/10.2514/1.23917>.
- , T. Gerz, F. Köpp, E. Stumpf, M. Harris, R. I. Young, and A. Dolfi-Bouteyre, 2003: Strategies for circulation evaluation of aircraft wake vortices measured by lidar. *J. Atmos. Oceanic Technol.*, **20**, 1183–1195, [https://doi.org/10.1175/1520-0426\(2003\)020%3C1183:SFCEOA%3E2.0.CO;2](https://doi.org/10.1175/1520-0426(2003)020%3C1183:SFCEOA%3E2.0.CO;2).
- , N. Tchipev, and A. Stephan, 2016: Wind impact on single vortices and counterrotating vortex pairs in ground proximity. *Flow Turbul. Combust.*, **97**, 829–848, <https://doi.org/10.1007/s10494-016-9729-2>.
- , and Coauthors, 2021: Mitigating wake turbulence risk during final approach via plate lines. *AIAA J.*, **59**, 4626–4641, <https://doi.org/10.2514/1.J060025>.
- Jacob, D., D. Y. Lai, M. J. Pruis, and D. P. Delisi, 2015: Assessment of WakeMod 4: A new standalone wake vortex algorithm for estimating circulation strength and position (invited). *7th AIAA Atmospheric and Space Environments Conf.*, Dallas, TX, AIAA, AIAA 2015-3176, <https://doi.org/10.2514/6.2015-3176>.
- Keye, S., 2011: Fluid-structure coupled analysis of a transport aircraft and flight-test validation. *J. Aircr.*, **48**, 381–390, <https://doi.org/10.2514/1.C000235>.
- Kundu, P. K., and I. M. Cohen, 2002: *Fluid Mechanics*. 2nd ed. Academic Press, 706 pp.
- Lamb, H., 1923: *Hydrodynamics*. 6th ed. Dover Publications Inc., 768 pp.
- Li, J., C. Shen, H. Gao, P. W. Chan, K. K. Hon, and X. Wang, 2020: Path integration (PI) method for the parameter-retrieval of aircraft wake vortex by lidar. *Opt. Express*, **28**, 4286–4306, <https://doi.org/10.1364/OE.382968>.
- Lugan, S., 2016: Geometry-based simulations for detection of wake vortices using a pulsed Doppler lidar. Ph.D. thesis, Université Catholique de Louvain, 154 pp., <https://hdl.handle.net/2078.1/178073>.
- Lundquist, J. K., M. J. Churchfield, S. Lee, and A. Clifton, 2015: Quantifying error of lidar and sodar Doppler beam swinging measurements of wind turbine wakes using computational fluid dynamics. *Atmos. Meas. Tech.*, **8**, 907–920, <https://doi.org/10.5194/amt-8-907-2015>.
- Manhart, M., 2004: A zonal grid algorithm for DNS of turbulent boundary layers. *Comput. Fluids*, **33**, 435–461, [https://doi.org/10.1016/S0045-7930\(03\)00061-6](https://doi.org/10.1016/S0045-7930(03)00061-6).
- Meneveau, C., T. S. Lund, and W. H. Cabot, 1996: A Lagrangian dynamic subgrid-scale model of turbulence. *J. Fluid Mech.*, **319**, 353–385, <https://doi.org/10.1017/S0022112096007379>.
- Meyer Forsting, A. R., N. Troldborg, and A. Borraccino, 2017: Modelling lidar volume-averaging and its significance to wind turbine wake measurements. *J. Phys.: Conf. Ser.*, **854**, 012014, <https://doi.org/10.1088/1742-6596/854/1/012014>.
- Ministère de la Transition Écologique et Solidaire, 2018: RECAT-EU for Paris–CDG & Le Bourge. Ministère de la Transition Écologique et de la Cohésion des Territoires, République Française Tech. Rep., 4 pp., https://www.ecologie.gouv.fr/sites/default/files/documents/RECAT_EU.pdf.
- Misaka, T., F. Holzäpfel, and T. Gerz, 2012: Wake evolution of wing-body configuration from roll-up to vortex decay. *50th AIAA Aerospace Sciences Meeting including the New Horizons Forum and Aerospace Exposition*, Nashville, TN, AIAA, <https://doi.org/10.2514/6.2012-428>.
- Moet, H., F. Laporte, G. Chevalier, and T. Poinsot, 2005: Wave propagation in vortices and vortex bursting. *Phys. Fluids*, **17**, 054109, <https://doi.org/10.1063/1.1896937>.
- Morris, C., J. Peters, and P. Choroba, 2013: Validation of the time based separation concept at London Heathrow Airport. *10th USA/Europe Air Traffic Management Research and Development Seminar*, Chicago, IL, National Air Traffic Services and EUROCONTROL, 1–41, <https://www.researchgate.net/publication/327466692>.
- Moser, R. D., J. Kim, and N. N. Mansour, 1999: Direct numerical simulation of turbulent channel flow up to $Re_\tau = 590$. *Phys. Fluids*, **11**, 943–945, <https://doi.org/10.1063/1.869966>.
- Oude Nijhuis, A. C. P., and Coauthors, 2018: Wind hazard and turbulence monitoring at airports with lidar, radar, and Mode-S downlinks: The UFO project. *Bull. Amer. Meteor. Soc.*, **99**, 2275–2293, <https://doi.org/10.1175/BAMS-D-15-00295.1>.
- Robey, R., and J. K. Lundquist, 2022: Behavior and mechanisms of Doppler wind lidar error in varying stability regimes. *Atmos. Meas. Tech.*, **15**, 4585–4622, <https://doi.org/10.5194/amt-15-4585-2022>.
- Robins, R., D. Delisi, and G. Greene, 2001: Algorithm for prediction of trailing vortex evolution. *J. Aircr.*, **38**, 911–917, <https://doi.org/10.2514/2.2851>.
- Rooseleer, F., and V. Treve, 2018: European wake turbulence categorisation and separation minima on approach and departure. EURO-CONTROL Tech. Rep., 28 pp., <https://www.eurocontrol.int/publication/european-wake-turbulence-categorisation-and-separation-minima-approach-and-departure>.
- Rye, B. J., 1990: Spectral correlation of atmospheric lidar returns with range-dependent backscatter. *J. Opt. Soc. Amer.*, **7A**, 2199–2207, <https://doi.org/10.1364/JOSAA.7.002199>.
- Salamitou, P., A. Dabas, and P. H. Flamant, 1995: Simulation in the time domain for heterodyne coherent laser radar. *Appl. Opt.*, **34**, 499–506, <https://doi.org/10.1364/AO.34.000499>.
- Schwaborn, D., T. Gerhold, and R. Heinrich, 2006: The DLR TAU-code: Recent applications in research and industry. *Proc. European Conf. on Computational Fluid Dynamics*, Egmond aan Zee, Netherlands, TU Delft, 1–25, <https://www.researchgate.net/profile/Dieter-Schwaborn/publication/224798567>.

- Simley, E., L. Y. Pao, R. Frehlich, B. Jonkman, and N. Kelley, 2014: Analysis of light detection and ranging wind speed measurements for wind turbine control. *Wind Energy*, **17**, 413–433, <https://doi.org/10.1002/we.1584>.
- Smalikho, I. N., 2019: Taking into account the ground effect on aircraft wake vortices when estimating their circulation from lidar measurements. *Atmos. Oceanic Opt.*, **32**, 686–700, <https://doi.org/10.1134/S1024856019060149>.
- , V. A. Banakh, F. Holzäpfel, and S. Rahm, 2015: Method of radial velocities for the estimation of aircraft wake vortex parameters from data measured by coherent Doppler lidar. *Opt. Express*, **23**, A1194–A1207, <https://doi.org/10.1364/OE.23.0A1194>.
- Spalart, P. R., M. K. Strelets, A. K. Travin, and M. L. Shur, 2001: Modeling the interaction of a vortex pair with the ground. *Fluid Dyn.*, **36**, 899–908, <https://doi.org/10.1023/A:1017958425271>.
- Stephan, A., 2014: Wake vortices of landing aircraft. Ph.D. thesis, Ludwig-Maximilians-Universität München, 163 pp., https://edoc.ub.uni-muenchen.de/16756/1/Stephan_Anton.pdf.
- , F. Holzäpfel, and T. Misaka, 2013: Aircraft wake-vortex decay in ground proximity—Physical mechanisms and artificial enhancement. *J. Aircr.*, **50**, 1250–1260, <https://doi.org/10.2514/1.C032179>.
- , —, and —, 2014: Hybrid simulation of wake-vortex evolution during landing on flat terrain and with plate line. *Int. J. Heat Fluid Flow*, **49**, 18–27, <https://doi.org/10.1016/j.ijheatfluidflow.2014.05.004>.
- , D. Rohlmann, F. Holzäpfel, and R. Rudnik, 2019a: Effects of detailed aircraft geometry on wake vortex dynamics during landing. *J. Aircr.*, **56**, 974–989, <https://doi.org/10.2514/1.C034961>.
- , N. Wildmann, and I. Smalikho, 2019b: Effectiveness of the MFAS method for determining the wind velocity vector from Windcube 200s lidar measurements. *Atmos. Oceanic Opt.*, **32**, 555–563, <https://doi.org/10.1134/S1024856019050166>.
- , G. Rotshteyn, N. Wartha, F. Holzäpfel, N. Petross, and L. Stietz, 2023: Artificial neural networks for individual tracking and characterization of wake vortices in lidar measurements. *AIAA AVIATION 2023 Forum*, San Diego, CA, AIAA, <https://doi.org/10.2514/6.2023-3682>.
- Thomson, J. A. L., and J. C. S. Meng, 1976: Scanning laser Doppler velocimeter system simulation for sensing aircraft wake vortices. *J. Aircr.*, **13**, 605–613, <https://doi.org/10.2514/3.44549>.
- Wartha, N., A. Stephan, F. Holzäpfel, and G. Rotshteyn, 2022: Characterizing aircraft wake vortex position and strength using lidar measurements processed with artificial neural networks. *Opt. Express*, **30**, 13 197–13 225, <https://doi.org/10.1364/OE.454525>.
- , —, F. N. Holzäpfel, and G. Rothsteyn, 2023: Investigating errors of wake vortex retrievals using high fidelity lidar simulations. *AIAA AVIATION 2023 Forum*, San Diego, CA, AIAA, AIAA 2023-3679, <https://doi.org/10.2514/6.2023-3679>.
- , —, and F. Holzäpfel, 2024: Virtual RHI lidar scans retrieved in high-fidelity wake vortex simulations of landing aircraft under turbulent crosswind conditions - LES Lidar Simulator (LLS). Zenodo, accessed 12 July 2024, <https://doi.org/10.5281/zenodo.12085035>.
- Wassaf, H. S., D. C. Burnham, and F. Y. Wang, 2011: Wake vortex tangential velocity adaptive spectral (TVAS) algorithm for pulsed lidar systems. *16th Coherent Laser Radar Conf.*, Long Beach, CA, Universities Space Research Association, 1–7, <https://rosap.ntl.bts.gov/view/dot/9150>.
- Wei, Z., T. Lu, R. Gu, and F. Liu, 2024: DBN-GABP model for estimation of aircraft wake vortex parameters using lidar data. *Chin. J. Aeronaut.*, **37**, 347–368, <https://doi.org/10.1016/j.cja.2024.05.011>.
- Zheng, Z. C., and R. L. Ash, 1996: Study of aircraft wake vortex behavior near the ground. *AIAA J.*, **34**, 580–589, <https://doi.org/10.2514/3.13107>.